· Article · Advances in Polar Science
doi: 10.13679/j.advps.2021.0006 June 2021 Vol. 32 No. 2: 118-140

Ocean stratification and sea-ice cover in Barents and Kara seas modulate sea-air methane flux: satellite data

Leonid YURGANOV[1*], Dustin CARROLL[2], Andrey PNYUSHKOV[3], Igor POLYAKOV[3] & Hong ZHANG[4]

[1] University of Maryland Baltimore County (ret), Baltimore, MD, USA;
[2] Moss Landing Marine Laboratories, San José State University, CA, USA;
[3] International Arctic Research Center, University of Alaska Fairbanks, AK, USA;
[4] Jet Propulsion Laboratory, California Institute of Technology, CA, USA

Received 31 March 2021; accepted 15 June 2021; published online 30 June 2021

Abstract The diverse range of mechanisms driving the Arctic amplification and global climate are not completely understood and, in particular, the role of the greenhouse gas methane (CH_4) in the Arctic warming remains unclear. Strong sources of methane at the ocean seabed in the Barents Sea and other polar regions are well documented. Nevertheless, some of those publications suggest that negligible amounts of methane fluxed from the seabed enter the atmosphere, with roughly 90% of the methane consumed by bacteria. Most in situ observations are taken during summer, which is favorable for collecting data but also characterized by a stratified water column. We present perennial observations of three Thermal IR space-borne spectrometers in the Arctic between 2002 and 2020. According to estimates derived from the data synthesis ECCO (Estimating the Circulation and Climate of the Ocean), in the ice-free Barents Sea the stratification in winter weakens after the summer strong stability. The convection, storms, and turbulent diffusion mix the full-depth water column. CH_4 excess over a control area in North Atlantic, measured by three sounders, and the oceanic Mixed Layer Depth (MLD) both maximize in winter. A significant seasonal increase of sea-air exchange in ice-free seas is assumed. The amplitude of the seasonal methane cycle for the Kara Sea significantly increased since the beginning of the century. This may be explained by a decline of ice concentration there. The annual CH_4 emission from the Arctic seas is estimated as 2/3 of land emission. The Barents/Kara seas contribute between 1/3 and 1/2 into the Arctic seas annual emission.

Keywords **satellite data, greenhouse gases, methane, Thermal IR (TIR), Arctic**

Citation: Yurganov L, Carroll D, Pnyushkov A, et al. Ocean stratification and sea-ice cover in Barents and Kara seas modulate sea-air methane flux: satellite data. Adv Polar Sci, 2021, 32(2): 118-140, doi: 10.13679/j.advps.2021.0006

1 Introduction

The Arctic has experienced the fastest warming on Earth over recent decades, with the Arctic Ocean warming at nearly double the rate of the global ocean (Hoegh-Guldberg and Bruno, 2010). The area, thickness, and concentration of sea-ice cover, has been significantly reduced (Comiso et al., 2008; Årthun et al., 2019). There is concern about the release of large amounts of the climate-active greenhouse gas methane (CH_4) from hydrates, permafrost, and other seabed reservoirs (James et al., 2016). The radiation warming potential of methane is 28–34 times that of carbon dioxide (CO_2) over a 100-year period (Myhre et al., 2013). The Barents and Kara seas (BKS) have extensive reserves of oil and natural gas (Shipilov and Murzin, 2002).

* Corresponding author, ORCID: 0000-0001-5984-3772, E-mail: leonid.yurganov@gmail.com

Thermogenic (fossil) methane penetrates through faults in sedimentary layers in the BKS. For example, Serov et al. (2017) reported on intensive cold seep activity clustered on the tops of several ~500-m-wide domes at depths of 370–390 m in Storfjordrenna, northwestern Barents Sea. A review article (James et al., 2016) describes the principal processes that regulate methane distribution in Arctic seafloor sediments, modification in the water column, and subsequent release to the atmosphere. Enhanced concentrations of dissolved methane in the Arctic Ocean seawater (Supplementary Figure S1) are widely observed (Gentz et al., 2014; Myhre et al.; 2016; Mau et al., 2017); these are related, in part, to direct seeps of thermogenic methane, dissociation of gas hydrates and thawing of submerged permafrost. Methane is slowly oxidized by methanotrophic bacteria in oceanic deep layers below the pycnocline with timescales of weeks or years (James et al., 2016). As noted by James et al. (2016), the effect of reduced sea-ice cover on ocean-to-atmosphere methane emissions are especially poorly constrained. The satellite measurements promise to fill this critical gap. Warm Atlantic currents make the BKS a climatically important region (Skagseth et al., 2020). A decline in BKS sea-ice in early winter influences synoptic processes across the northern hemisphere (Petoukhov and Semenov, 2010; Årthun et al., 2019). The Barents Sea is a shallow sea (average depth 230 m), with depressions up to 400 m. The Kara Sea is even shallower (average depth ~100 m). The release of methane from the seabed as a result of degradation of the submarine permafrost (Portnov et al., 2014) is expected in the Kara and southern Barents seas. The most of Barents Sea is free of sea-ice year-round, while winter sea-ice cover in the Kara Sea, as well as in the northernmost Barents Sea, underwent a dramatic decline since early 2000s (Zhang et al., 2018b).

The presence of sources is just one necessary condition for methane to enter the atmosphere; transport of the gas from the seafloor to the ocean surface is also critically important. According to Rudels (1993), the relatively warm and salty layer of Atlantic Water (AW) provides a stratified barrier that can inhibit the penetration of dissolved gases into the ocean-surface layer during summer/early autumn (between June and October). Numerous direct studies have shown that during this season the flux in the Barents-Svalbard area is negligible (Gentz et al., 2014; Myhre et al., 2016; Mau et al., 2017). These field investigations, however, also identified strong sources at the seafloor and large concentrations of dissolved methane in deep ocean waters. Therefore, the flux of methane may be significant only after a breakdown of the pycnocline in November, and subsequent growing of the Mixed Layer Depth (MLD). The MLD increases sharply in November, with the bulk of the Barents Sea water column mixed by December (Kara et al., 2002). Increased diffusion is expected to facilitate methane fluxes to the atmosphere.

Methane over the BKS was measured from space by IASI (Infrared Atmospheric Sounding Interferometer) and AIRS (Atmospheric InfraRed Sounder) spectrometers (Yurganov et al., 2016a, 2016b, 2016c, 2017; Yurganov, 2020). Maps of monthly mean low tropospheric (LT) Arctic methane concentrations, retrieved from the IASI-1 orbital measurements for 2013, have been presented by Yurganov et al. (2016a) and for 2018 by Yurganov (2020). Preliminarily, Yurganov et al. (2016a) assessed the annual Arctic Ocean CH_4 emissions in 2010–2014 as ~ 2/3 of land CH_4 emission for North of 60 ° N. Satellite observations in the Thermal IR (TIR) range are extremely useful for characterizing methane over ocean regions, particularly during the polar night. Other observational approaches, such as space-borne Short-Wave IR sensors (e.g., TROPOMI, the TROPOspheric Monitoring Instrument) require sunlight and cannot make observations during the polar night (attached Supplementary Figure S2). Additionally, ship-based observations are logistically challenging in these ice-choked regions. Here we analyze methane concentrations in the lowest tropospheric layer over BKS estimated from three TIR sounders: AIRS/Aqua, IASI-1/MetOp-A, and Cross-Track Infrared Sounder (CrIS) deployed on the Suomi National Polar-orbiting Partnership (SNPP). These data are coupled with regular satellite microwave measurements of sea-ice concentration, described by Cavalieri et al. (1996). MLD and near-bottom temperatures were supplied from the "Estimating the Circulation and Climate of the Ocean" (ECCO) consortium (Wunsch et al., 2009) ocean state estimate.

2 Methods

2.1 Satellite instruments, methane data, and retrieval techniques

AIRS, IASI, and CrIS belong to the TIR group of hyper-spectral sounders (their characteristics are listed by Smith and Barnet (2019)). An important advantage of them is a capability to work at night and over water surface. A disadvantage is a reduced sensitivity to lower troposphere (Smith and Barnet, 2020). E.g., the sensitivity for atmospheric 0–4 km layer is just a half of that for middle troposphere (Yurganov et al., 2016a). This should be taken in account during the analysis of measurements.

The AIRS diffraction grating spectrometer was launched in a sun-synchronous polar orbit in May 2002 on board the Aqua satellite (Xiong et al., 2008). The instrument scans ± 48.3 ° from the nadir, which provides full daily coverage in the Arctic. Spectral resolution is 1.5 cm^{-1} at the methane ν4 absorption band near 7.65 μm. Currently (May, 2021), the AIRS is still operational. Starting in September 2002, methane data were processed consistently using version 6 of the standard algorithm developed by NASA (Susskind et al., 2014). A new improved version 7 of the data (Tian et al., 2020; Yue and Lambrigtsen, 2020) is characterized by: improved consistency between day and

night water vapor, improved temperature products, improved AIRS IR only retrievals, especially in the high latitude regions, removal of ambiguity in surface classification in the infrared-only (IR-only) retrieval algorithm. Monthly average Level 3 methane, surface and air temperatures between October 2002 and January 2020, both ascending and descending orbits, are available on-line on a 1 ° × 1 ° latitude/longitude grid: https://disc.gsfc.nasa.gov/datasets/, AIRS3STM.006 and AIRS3STM.007 for versions 6 and 7, respectively. Methane profiles were retrieved for a 3 × 3 matrix of 9 pixels with a diameter of 13.5 km in nadir each. Below the AIRS version 7 is used, unless otherwise noted.

The IASI-1/MetOp-A is a cross-track-scanning Michelson interferometer that measures spectra of outgoing long wave radiation with an apodized resolution of 0.5 cm^{-1} in the TIR spectral range that includes the ν4 CH_4 band near 7.65 μm wavelength (Razavi et al., 2009). The MetOp-A satellite, operated by EUMETSAT (European Organisation for the Exploitation of Meteorological Satellites), was launched in 2006. Like AIRS, IASI has a 2200-km swath with a scan swath angle of ±48.3 °. The IASI retrieval algorithm NUCAPS (NOAA Unique Combined Atmospheric Processing System) was built at NOAA/ NESDIS (National Environmental Satellite, Data, and Information Service) to emulate the AIRS Version 5 code and has been in operation since 2008 (Maddy et al., 2009; Gambacorta, 2013). Level 2 data for 2 × 2 matrices of 4 circular, 12-km diameter pixels are available from the NOAA's CLASS (Comprehensive Large Array-data Stewardship System) site https://www.avl.class.noaa.gov/saa/products/.

The CrIS is a cross-tracking Michelson interferometer deployed on the Suomi NPP platform launched in October, 2011, in a sun-synchronous polar orbit (Bloom, 2001)). Apodized full spectral resolution is 0.75 cm^{-1}. Methane profiles were obtained for a 3 × 3 matrix of 9 pixels with a diameter of 14 km in nadir each. Retrieval technique CLIMCAPS (Community Long-Term Infrared Microwave Combined Atmospheric Product System) was developed in Science and Technology Corporation (STC), Columbia, MD, and funded by NASA (Smith and Barnet, 2019, 2020). Assimilated air temperature and humidity from Modern-Era Retrospective Analysis for Research and Applications version 2.0 (MERRA2) were used as a priori. The Level 2 data coded as SNDRSNIML2CCPRET are available from the GES DISC (Goddard Earth Sciences Data and Information Services Center), https://disc.gsfc.nasa.gov/datasets/SNDRSNIML2CCPCCR_2/summary.

The TIR reliable measurements require the surface to be warmer than air above it. The data were filtered for cases of Thermal Contrast $ThC > 10$ ° C (Yurganov et al., 2016a and Supplementary Figure S3), where $ThC = T_{surf} - T_{600}$, T_{surf} is surface temperature (Surface Skin Temperature, *SST*), and T_{600} is air temperature at 600 hPa air pressure. Supplementary Figures S3 and S4 in the Supplement illustrate influence of filtering for AIRS v6 data.

The profiles were averaged for the lower troposphere (LT) from the surface to the level of 600 hPa (~ 4 km) and from 600 hPa to 400 hPa (~4–6 km, mid troposphere, MT). The sensitivity to methane variations in the LT and MT was estimated empirically by comparison with simultaneous aircraft measurements at three stations in the United States (Yurganov, 2020, and Supplementary Figure S5). LT sensitivity (slope of a linear regression line) was found in the range of 0.3–0.5. MT sensitivity was estimated as 0.8–1.2, i.e., significantly higher. A physical meaning of the empirical sensitivity is a change in retrieved concentration that corresponds to the unit change of the "true" value, measured from an aircraft. E.g., the sensitivity of 0.5 means that real variations (not concentrations themselves) are underestimated by 100%. We have chosen to focus on the LT data in attempt to get information on methane as close as possible to the surface despite their lower sensitivity. The MT CH_4 measured from satellite is rapidly carried by winds and is just slightly dependent on regional sources. However, some MT data are placed in the Supplement (Figures S6, S7, and S8).

2.2 Estimates of MLD and seawater temperature

The MLD characterizes degree of the vertical mixing in the seawater column. To estimate the MLD, we use the ECCO LLC270 global ocean and sea-ice data synthesis (Zhang et al., 2018a). ECCO LLC270 is built upon two previous ECCO efforts, ECCO v4 (Forget et al., 2015) and ECCO2 (Menemenlis et al., 2005a, 2005b, 2008; Fenty et al., 2017). Compared to the lower-resolution ECCO v4 synthesis (nominal 1 ° grid spacing), ECCO LLC270 has finer horizontal grid spacing (~1/3 ° at the equator and ~18 km at high latitudes). The vertical discretization comprises 50 *z*-levels; model integration spans January 1992 to December 2018. Terrestrial runoff along coastal boundaries is forced using the monthly climatology of Fekete et al. (2002). Since horizontal resolution is insufficient to resolve mesoscale eddies, their impact on the large-scale ocean circulation is parameterized using the Redi (1982) and Gent and McWilliams (1990) schemes.

We compute monthly-mean LLC 270 MLD using two criteria: (1) when the potential density is larger than surface-ocean density ρ by 0.8°C·α, where ρ is the density and α is the seawater thermal expansion coefficient at the ocean surface (Kara et al., 2000); and (2) when the potential density is greater than surface-ocean density + 0.03 kg m^{-3} (Boyer et al., 2004). Kara et al. (2002) compared calculations by criterion #1 with field measurements and confirmed that method accuracy is better than 20 m. Potential temperature of the lowest ECCO layer was treated as near-bottom temperature.

2.3 Satellite sea-ice observations

Sea-ice concentration data are archived by the NASA National Snow and Ice Data Center Distributed Active

Archive Center (https://nsidc.org/data/NSIDC-0081/versions/1; described by Cavalieri et al., 1996). The mean monthly data set for November, 2003–January, 2020 is generated from the surface brightness temperature data and is designed to provide a consistent time series of sea-ice concentration C_{ice} (the fraction of ice for each 20 × 20 km^2 pixel) spanning the coverage of two passive microwave instruments developed as a part of the Defense Meteorological Satellite Program (DMSP), DMSP-F8 and Special Sensor Microwave Imager/Sounder (SSMIS) DMSP-F17.

3 Results

3.1 CH_4 concentrations, trends and seasonal changes

To illustrate changes in CH_4 low tropospheric concentrations for 15 years, seasonal means for 2004 –2005 (Figure 1a–1d) and for 2019–2020 (Figure 1e–1h), retrieved from AIRS data, were mapped. CH_4 concentrations are subjected to global trend (Nisbet et al., 2019; Saunois et al., 2020), the trend of satellite LT data is ~3 ppb a^{-1} (Yurganov et al., 2017). Therefore, all color scales for the top four maps were shifted down by 45 ppb to make the bottom and top maps comparable. The data were binned into 3-month seasons, conditionally named "spring" (Feb–Apr), "summer" (May–Jul), "autumn" (Aug–Oct), and "winter" (Nov–Jan). This choice was motivated by the CH_4 seasonal cycle: "winter" is close to its maximum and "summer" is to its minimum (Supplementary Figure S8). The same color at the top and bottom maps of Figure 1 corresponds to 45 ppb difference between concentrations. The summer methane distributions over the Arctic (Figures 1b and 1f) were essentially flat; this may be interpreted as lacking strong local Arctic sources.

Quite different picture is observed in other seasons, especially in winter (Figures 1d and 1h). Enhanced CH_4 concentrations were observed over BKS and other seas. These anomalies may indicate significant regional sources. Moreover, concentrations over many areas increased significantly faster than by 3 ppb a^{-1}. Similar patterns were observed for MT altitudes (between 4 and 6 km, Supplementary Figures S5 and S6). To study seasonal changes and trends, three domains were selected (Figure 1 and Supplementary Table S1). Domain #1 is located in a relatively deep western Barents Sea (mean depth 379 m) and is free of sea ice year-round. Domain # 2 is located in northern Kara Sea between three archipelagos: Franz-Joseph Land (FJL), Novaya Zemplya (NZ), and Severnaya Zemlya (SZ). It is shallower (mean depth 180 m)

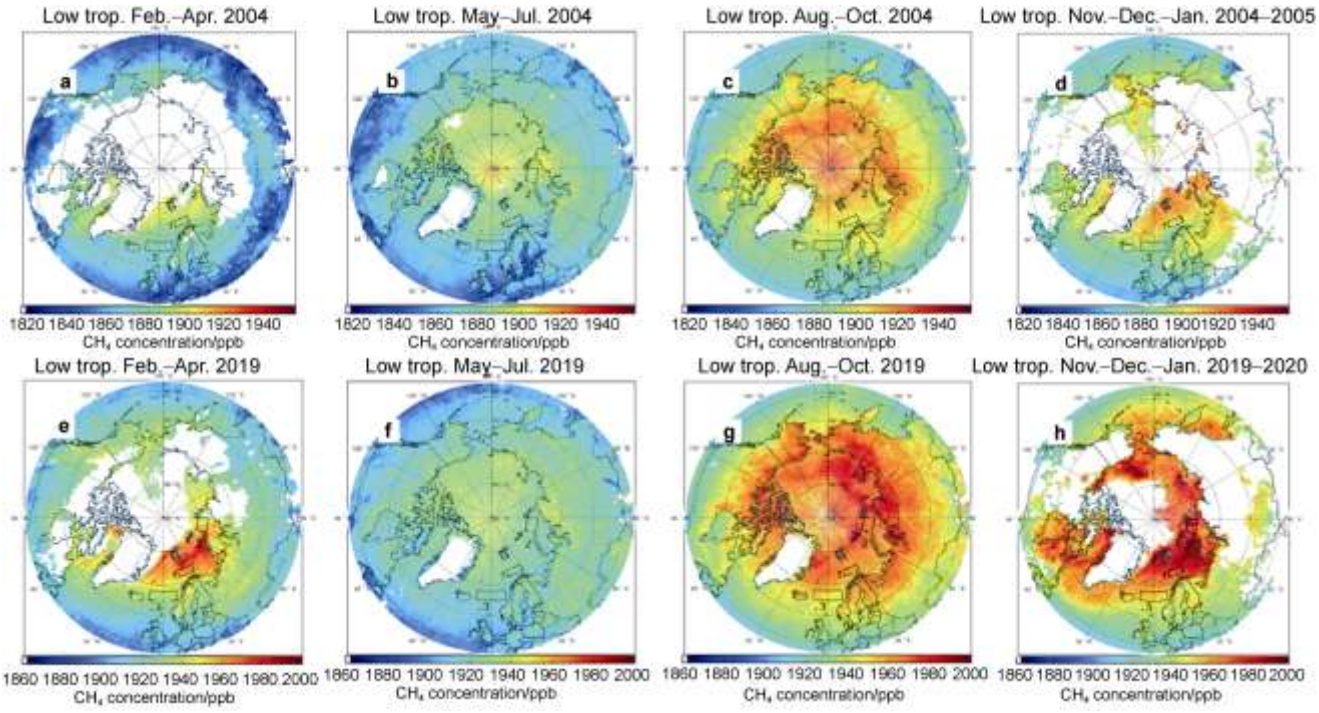

Figure 1 Methane concentrations retrieved from AIRS v7 data for the layer 0–4 km (LT) for 4 seasons: spring (**a**), summer (**b**), autumn (**c**), winter (**d**) for 2003–2004 (top) and 2019–2020 (bottom). Blank areas correspond to insufficient vertical air temperature contrast (ThC<10°C). Note a 45 ppb shift in the color scale, corresponding to 3 ppb·a^{-1} global trend. See also the same for MT (Supplementary Figure S6).

and partially covered by sea ice in winter. A control ice-free domain #3 with mean depth 2053 m is selected beyond the Arctic in the Norwegian Sea.

An excess of methane concentration in the domain #1 over that in the control domain #3 may be compared with the intensity of mixing in the seawater column, characterized by the MLD. Monthly mean concentrations for domains # 1 and # 3 were retrieved from data of three space-borne spectrometers and averaged over 2015–2019. Four independent data sets in Figure 2 corresponding to AIRS (versions 6 and 7), IASI, and CrIS are in agreement. All four series demonstrate a maximum in December–January and a minimum in June–July. The MLD was estimated using two different criteria (see Section 2.2) and averaged over the same time period for domain #1. These MLD curves have similar shapes, but somewhat different magnitudes, which might be taken as an estimate of data accuracy. Disagreements do not exceed 50 m (cf., MLD accuracy was estimated as ± 20 m by Kara et al. (2002) for the data based on criterion #1). Methane anomaly steeply grows in October–November and reaches a maximum in January. The mixed layer is very shallow in summer (~20–30 m), its depth abruptly increases between November and December, and plateaus by February. This is mostly explained by the autumn breakdown of seasonal pycnocline (Rudels, 1993), caused by decline in solar radiation and cooling of the surface layer. Seasonal changes in CH_4 anomalies most likely occur in response to changes in the seawater mixing. This will be discussed below in more detail in relation to MLD trends.

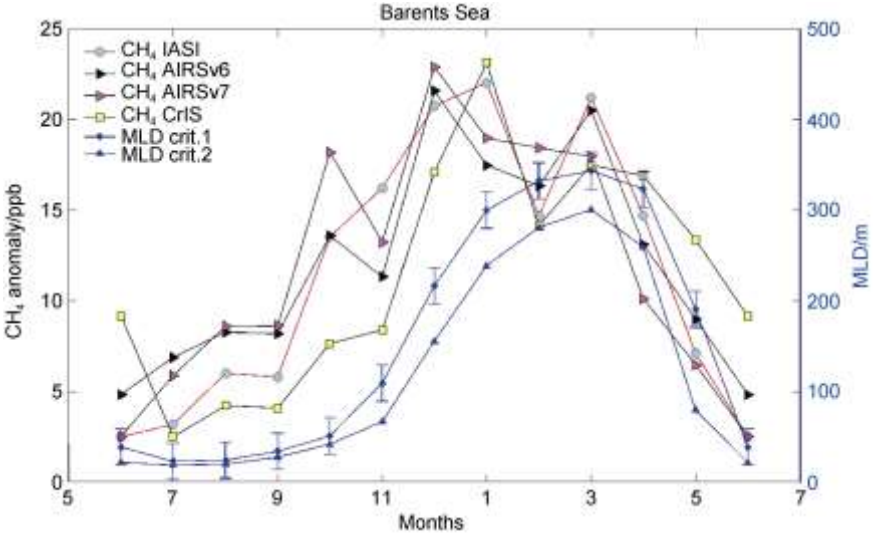

Figure 2 LT (0–4 km altitude) CH_4 anomaly, i.e., a concentration difference between the Barents Sea domain #1 and Norwegian Sea domain #3 (for boundaries see map Figure 1 and Supplementary Table S1). IASI and AIRS data are averaged over 2010–2018, CrIS data are for 2015–2018. Blue lines are 2010–2018 averaged MLD for the western Barents Sea domain #1 (see map) for 2 criteria (#1 is Kara et al. (2000) , #2 is Boyer et al. (2004).

Maps of seasonally resolved trends of CH_4 for 2003–2019 time frame are presented in Figure 3. In summer (Figure 3b) CH_4 trend over the whole Arctic Ocean is generally close to or even slightly lower than 3 ppb a^{-1}. Arctic land is characterized by 3.5–4 ppb a^{-1} trend. In autumn (August–October) trends are higher everywhere, but maximal trends are observed in winter over sea: typically, 4.5–5 ppb a^{-1} and even higher. The maximal rate of the long-term winter LT methane growth, up to 5.5 ppb a^{-1}, was found in the northern Kara Sea that was almost twice as large compared to the summer trend.

Figure 4 shows monthly mean methane concentrations for three domains (thin black lines) for two instruments: AIRS (version 7) and IASI. Slopes of seasonal linear least square correlation lines are labeled in the figures with lower and upper confidence limits for reliability 95%. For all domains winter trends are higher than summer trends, but the difference between them is statistically significant for the Kara Sea only (Figure 4c and 4f). IASI data are available only since 2010 only. A steeper growth detected by IASI may be explained a 3-fold better spectral resolution. A sea ice decline, observed during last two decades in the Kara Sea, may explain this effect, at least partly (see below).

3.2 Annually averaged CH_4 anomalies and emission estimates

Yurganov et al. (2016a) suggested an estimate of annually averaged methane emission from the Arctic seas based on assumption that anomalies averaged over 2010–2014 are proportional to annual emission. The "first guess" CH_4 concentration (Susskind et al., 2014; Smith and Barnet, 2019) was common for AIRSv6, AIRSv7, IASI/NUCAPS,

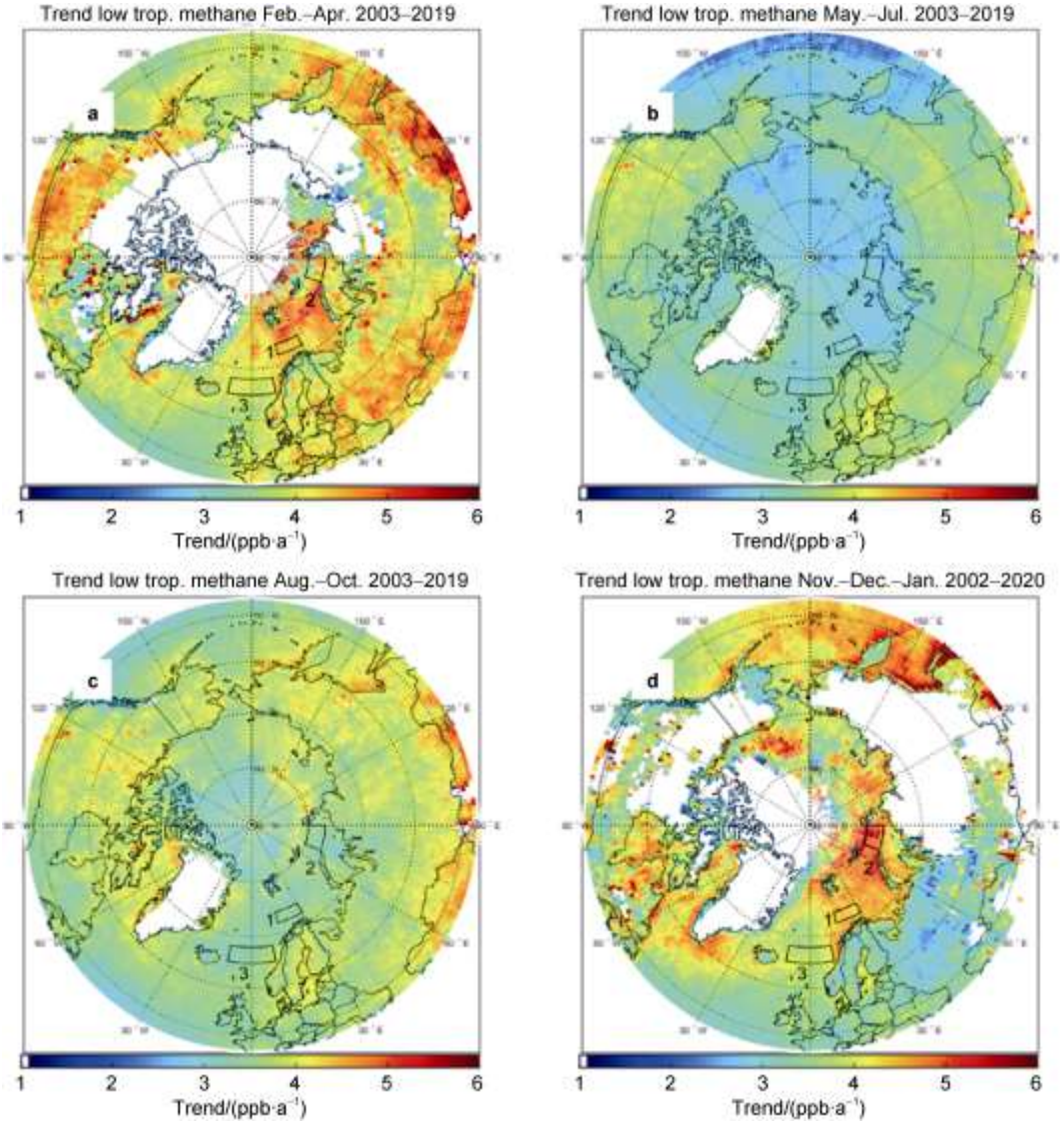

Figure 3 Maps of LT methane trends derived from 2002–2019 data of AIRS v7. Slopes of standard linear regression lines for 4 seasons: spring (**a**), summer (**b**), autumn (**c**), winter (**d**) were computed for each 1 °×1 ° lat/lon pixel. Blank areas correspond to insufficient vertical air temperature contrast (ThC<10°C). See also the same for MT (Supplementary Figure S7).

and CrIS/CLIMCAPS algorithms. The first guess was assumed the same for all longitudes and seasons and depending just on altitude and longitude. The West Siberian Lowland (WSL) was taken by Yurganov et al. (2016a) as a control area with "known" emission 22 Tg CH_4 a^{-1} (Fung et al., 1991). Here we averaged CH_4 anomalies for 2016–2020 period that is common for 3 instruments. The time elapsed after the previous study required an adjustment of the background for the CH_4 trend. For each instrument the latitudinally dependent first guess for 0–4 km layer was adjusted to the measured zonally averaged concentration and used as background for all longitudes (Supplementary Figure S10). Another difference with Yurganov et al. (2016a) calculation is using the total Arctic land as a control area with "known" annual emission (Saunois et al., 2020).

Three maps of anomalies are plotted in Figure 5 (top row). Following Yurganov et al. (1996a), these anomalies were converted to annually averaged flux density F (Figure 5, top row, lower scale and Figure 5, bottom row) for each instrument. Total annual Arctic land emission was assumed by Saunois et al. (2020) as E=25 Tg CH_4 a^{-1} for the area 18.2 × 10^6 km^2. It corresponds to the mean flux density F= 3.8 mg m^{-2} d^{-1}. Mean CH_4 anomalies for Arctic land are different for different instruments (Table 1). Therefore, conversion coefficients from ppb to mg m^{-2} d^{-1} for AIRS v7, IASI, and CrIS were different, namely 0.28, 0.19, and 0.29, respectively. The total annual emissions were summarized in Table 1 and Figure 6. Domains' boundaries are indicated in Figure 6 and listed in

Supplementary Table S1. Mean flux densities for domains, as well as minimal and maximal values inside domains are presented in Table 2. Our previous estimate for pan-Arctic sea emission as ~2/3 of land emission (Yurganov et al., 2016a) was confirmed. The BKS contributes between 1/3 and 1/2 into the total emission from seas. Available from literature top-down and bottom-up flux estimates for some domains are discussed below.

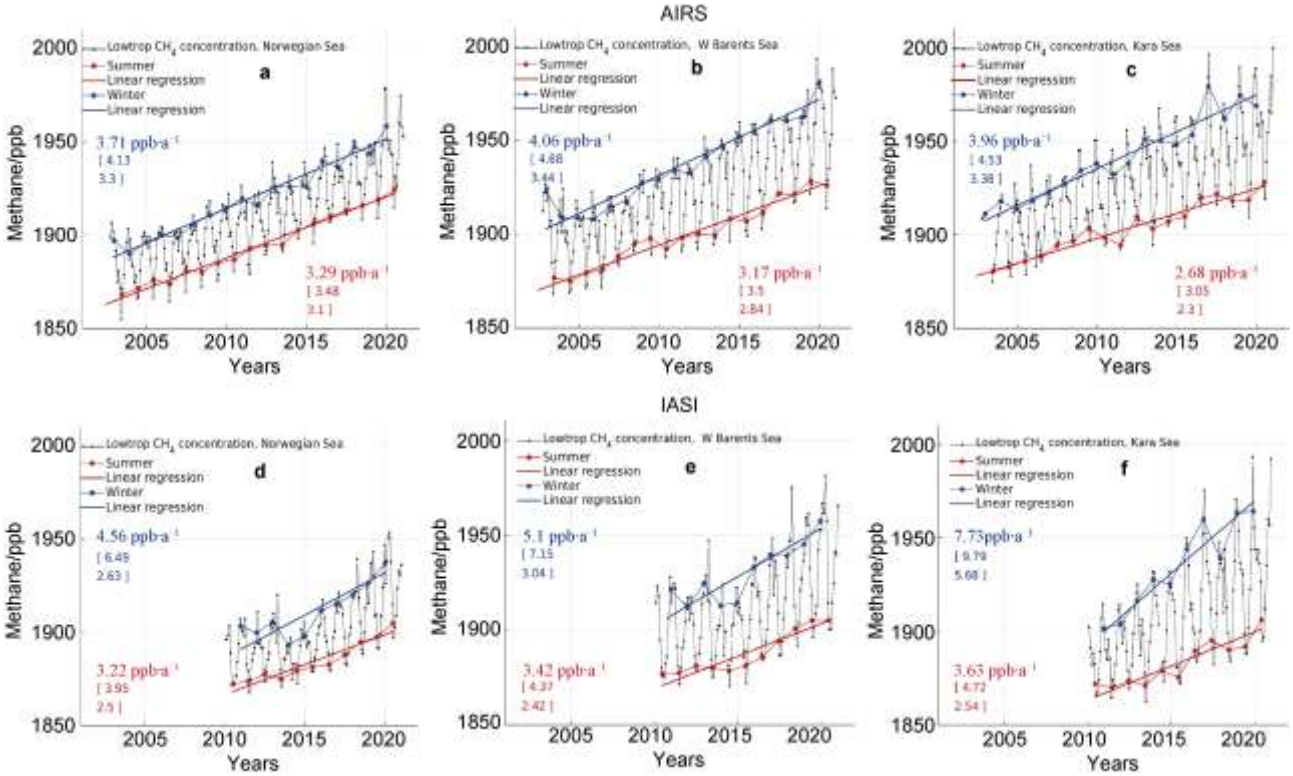

Figure 4 Methane LT concentrations and trends according to AIRS data (**a**, **b**, **c**) and IASI data (**d**, **e**, **f**) for three domains. Regression lines are plotted for winter and summer periods, slopes and 95% confidence limits (in brackets) are shown. Note that the increase in amplitude is statistically significant for the Kara Sea only.

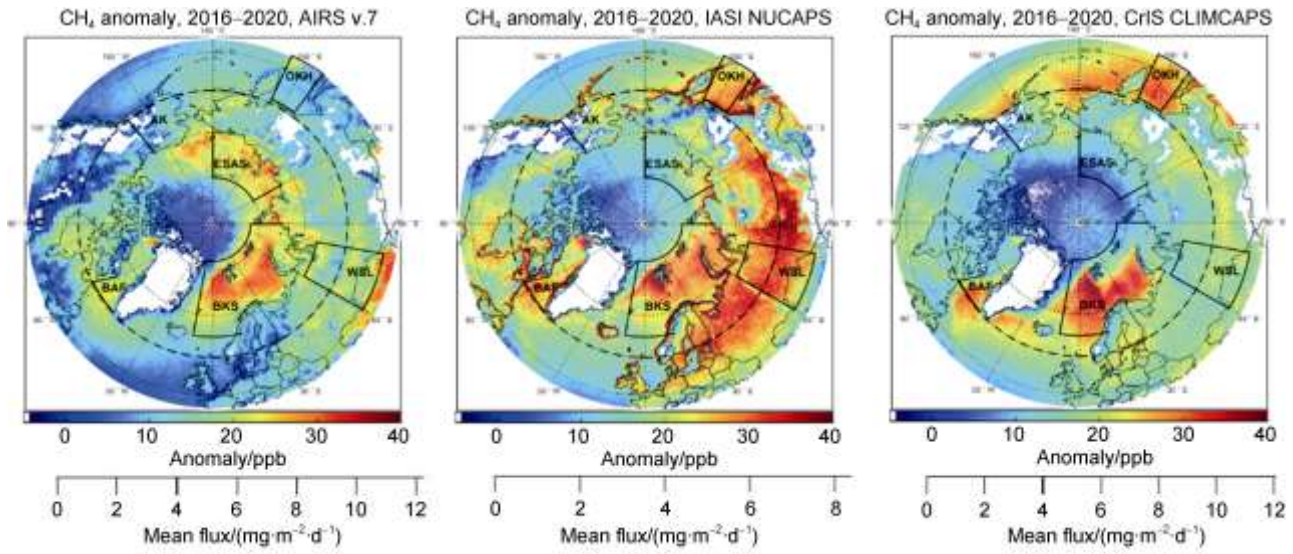

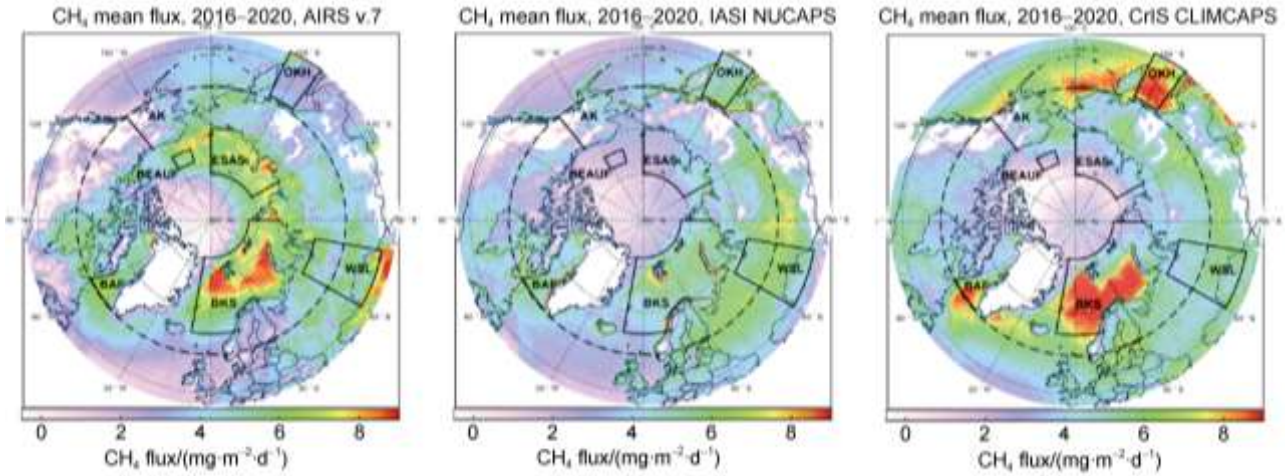

Figure 5 Top row: averaged for 2016–2020 CH_4 excess over background (Supplementary Figure S1). Bottom row: estimated fluxes for 3 instruments. Dashed line is the Arctic boundary.

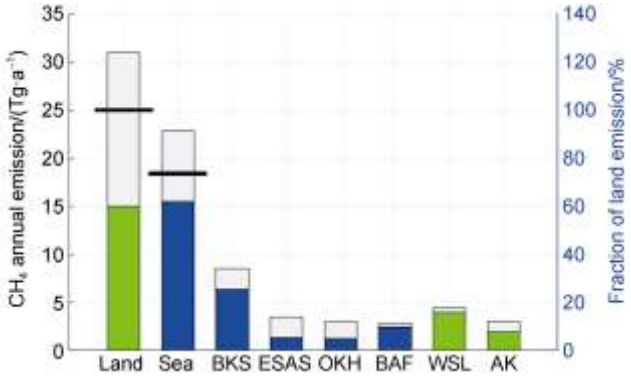

Figure 6 Annual emissions estimated for selected domains (green is for land, blue is for sea): Barents/Kara seas (BKS), East Siberian Arctic seas (ESAS), Sea of Okhotsk (OKH), Baffin Bay (BAF), West Siberian Lowland (WSL), and Alaska (AK). Land and Sea are for the Arctic to the North of 60 ° N. Uncertainty ranges of estimates for different instruments are shown in grey (see also Table 1).

3.3 Trends in MLD and temperature

Here and in Supplementary Figure S11 we present available auxiliary MLD, near-bottom temperature and sea ice data for BKS and for the control domain in the Norwegian Sea. As we did see above (Figure 2), the spacial CH_4 anomaly over the western Barents Sea increases sharply since November and reaches maximum in January. A most likely reason for that is a breakdown of the pycnocline in November and transfer from the summer density stratification to the winter mixing regime (Rudels, 1993). ECCO data allow to estimate changes in MLD during last two decades (Figure 7). MLD is subjected to a strong seasonality with a minimum of 20–30 m in summer and a maximum up to 350 m in winter. That means a well mixing of the Barents Sea from the surface down to the seafloor in winter. Red points correspond to a period of CH_4 anomaly maximum in early winter; green points are for the following three months. Early winter MLD diminished from 300 m in early 2000s down to 150 m now. In February–April

Table 1 Annual CH_4 flux, estimated from CH_4 LT anomalies in assumption of 25 Tg CH4 a^{-1} for the Arctic land to the North of 60 ºN. Anomaly of LT concentration is a difference between retrieved and background concentrations (for background definition see Supplementary Figure S9)

Domain	Area/($\times 10^6$ km^2)	CH_4 anomalies/ppb			CH_4 annual flux/(Tg CH_4 a^{-1})		
		AIRS	IASI	CrIS	AIRS	IASI	CrIS
Land	18.2	13.4	19.4	13.1	25.0	25.0	25.0
Sea	12.8	17.3	17.0	12.6	22.8	15.5	16.9
BKS	3.4	24.3	26.3	23.5	8.5	6.4	8.4
ESAS	1.4	23.7	15.7	8.9	3.5	1.6	1.3
OKH	1.0	11.9	26.1	29.0	1.2	1.8	3.0
BAF	1.4	19.4	24.9	19.8	2.7	2.4	2.8
WSL	2.2	18.7	28.7	17.4	4.2	4.5	4.0
AK	1.7	11.3	18.4	16.5	2.0	2.2	3.0

Table 2 Annually averaged CH_4 flux density for domains. Minimal and maximal flux are for grid cells 1°×1° (AIRS), 0.5°×0.5°(IASI and CrIS)

	AIRS	IASI	CrIS
BKS	6.8	5.1	6.7
min	1.0	1.3	0.4
max	9.8	9.7	11.8
ESAS	6.7	3.2	2.8
min	3.9	1.3	–1.1
max	9.5	6.3	5.7
BEAUF	6.1	2.4	2.5
min	4.7	1.3	0.3
max	8.3	3.1	4.8
BAF	5.4	4.8	5.7
min	2.6	3.2	2.5
max	7.9	8.3	9.5
OKH	2.7	5.4	8.3
min	1.9	4.4	6.5
max	3.3	6.4	9.5
AK	3.1	3.4	4.6
min	0.4	–1.6	–0.2
max	6.0	7.8	8.9
WSL	5.3	5.6	5.0
min	2.1	2.2	1.9
max	8.8	7.2	7.7

Units: mg CH_4 m^{-2} d^{-1}

decrease of MLD was not so steep. The steepest decline of -10 ± 3 m a^{-1} was observed in November (Supplementary S10). In Figure 7b MLD seasonal cycles for the beginning and for the end of the considered period were compared. The late autumn-early winter part of the cycle (November–January) shifted by 5 weeks to later times during elapsed 15 years. The negative MLD trend in early winter may hamper the process of CH_4 transfer from the seabed to the surface. Meanwhile, no statistically significant MLD trends for other domains were observed (Supplementary Figure S10).

The temperature of the near-bottom seawater layer is important for CH_4 release from methane hydrates (James et al., 2016). Figure 8 evidences a statistically significant upward trend of 0.05–0.06 ℃ a^{-1} after 1992. Also, there is a statistically significant difference in trends between periods 1965–1992 and 1992–2017. In contrast to the Barents Sea, two other domains demonstrate much lower temperatures that are pretty constant during last 30 years.

4 Discussion

4.1 Comparisons with in situ CH_4 observations and models.

Shakhova et al. (2010) investigated summer and winter methane flux from the East Siberian Arctic Seas (ESAS). More than 5000 at-sea measurements of dissolved CH_4 were collected. Greater than 80% of ESAS bottom waters and greater than 50% of surface waters were supersaturated with CH_4 relative to the atmosphere. In summer, diffusion and ebullition fluxes were estimated, respectively, as 1.24 Tg CH_4 and 1.68 Tg CH_4 (total summer 2.92 Tg CH_4), in winter 3.23 Tg CH_4 and 4.49 Tg CH_4 (total winter 7.72 Tg CH_4), totally 10.64 Tg CH_4 a^{-1}. An assessment by Berchet et al. (2016) based on land surface NOAA network and inverse modeling was significantly lower: 0.5–4.3 Tg CH_4 a^{-1}. Our estimate 1.3–3.5 Tg CH_4 a^{-1} is inside the Berchet et al. (2016) range.

CH_4 measurements in the aircraft Carbon in Arctic Reservoirs Vulnerability Experiment (CARVE) in May–October of 2012, 2013, and 2014 (Miller et al., 2016) demonstrated little year-to-year variability in the fluxes. The total Alaska CH_4 fluxes average 1.74 ± 0.26 Tg CH_4 for 6 months that is close to our estimate of 2–3 Tg CH_4 a^{-1}.

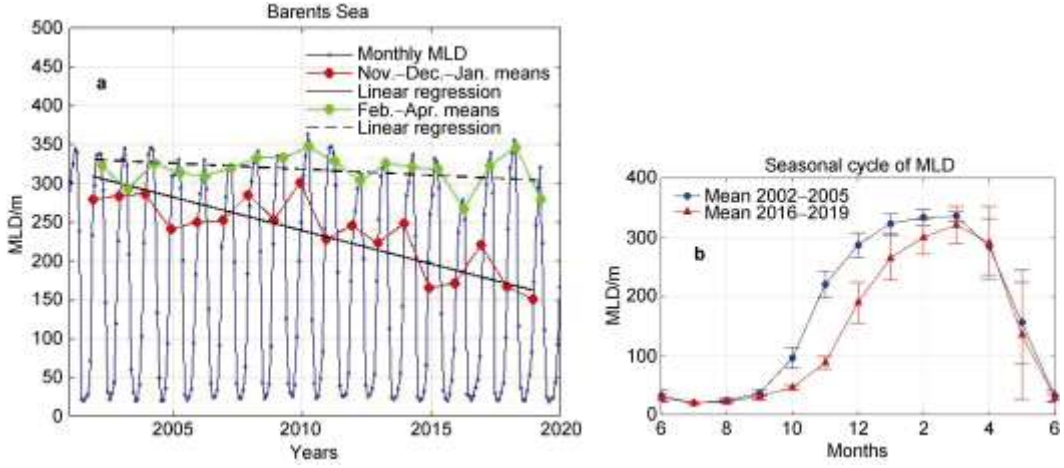

Figure 7 **a**, Monthly and seasonally averaged MLD for domain #1. The seasons are the same as for CH_4 (Figures 1 and 3); **b**, Seasonal cycles for beginning and end of the data span.

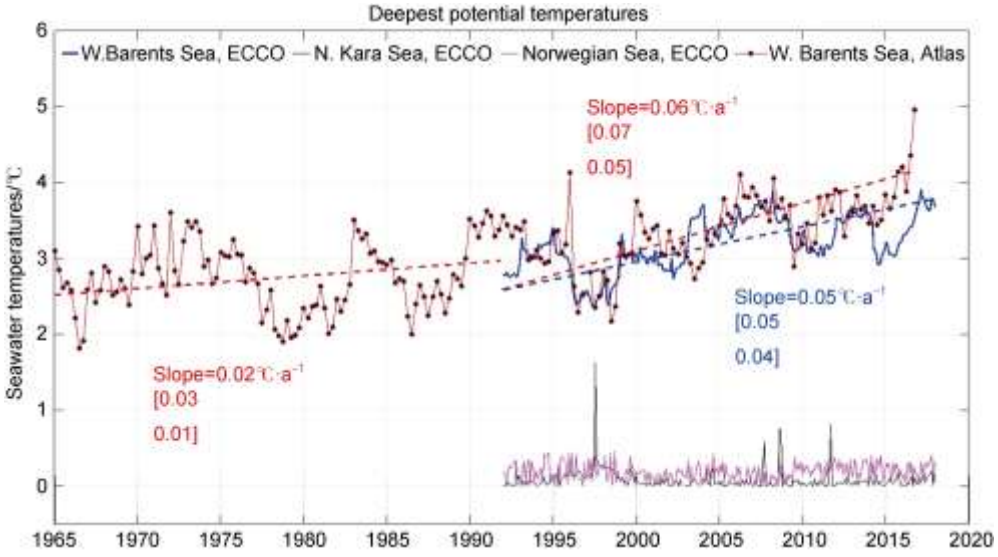

Figure 8 Monthly mean near-bottom potential temperatures for three domains considered in this study according to ECCO and the Atlas of oceanography data for the Barents Sea (Watelet et al., 2020). Slopes of linear regression lines with lower and upper confidence limits for reliability 95% (square brackets) are shown.

The WSL CH_4 emission is highly uncertain. The inventory EDGAR v4.3.2 (Janssens-Maenhout et al., 2017) predicts a total leaks of natural gas in western Siberia of 2.8 Tg CH_4 a^{-1}, whereas ECLIPSE v5a (Höglund-Isaksson et al., 2012) yields 14.1 Tg CH_4 a^{-1}. The wetland emission bottom-up estimate is 3.9 ± 1.3 Tg CH_4 a^{-1} (Glagolev et al., 2011). The top-down estimates are uncertain also, e.g., Berchet et al. (2015): 5–28 Tg CH_4 for the year 2010. In any case, our estimate 1.3–3.5 Tg CH_4 a^{-1} is close to or below than available lowest estimates. Our estimates in Table 1 are based on assumed 25 Tg CH_4 a^{-1} for the Arctic land, and spectroscopic data, as it was noted above, are biased to lower values. Also winter is missing: it is a reason for underestimation as well. Supplementary Figure S12 shows a flat coverage for all seasons for BKS, but all other domains are characterized by reduced number of measurements in January, February, November and December.

Some random measurements of CH_4 flux may be compared with our annual means (Table 2). There were measurements of CH_4 flux in the Beaufort Sea in January 2009, in November 2009 and in March–April 2010 by Kort et al. (2012); 0.5–8.0 mg CH_4 m^{-2} d^{-1} with a mean of 2.0 mg CH_4 m^{-2} d^{-1}. These data are very close to our estimates for the Beaufort Sea: mean annual values for different sounders between 2.4 and 6.1 mg CH_4 m^{-2} d^{-1} and the total range: 0.3–8.3 mg CH_4 m^{-2} d^{-1}.

Myhre et al. (2016) studied CH_4 near the seafloor and in the atmosphere to the west of Svalbard in June–July 2014. They found that the release of CH_4 from seabed sediments substantially increases CH_4 concentrations near the seafloor with a sharp decrease above the pycnocline. The summertime flux to air was estimated as 2.4–14 nM m^{-2} s^{-1}, i.e., less than 0.02 mg CH_4 m^{-2} d^{-1}.

Lorenson et al. (2016) reported results of flux measurements in 1992–2009 during July–September seasons in the Beaufort Sea. During ice-free periods, CH_4 flux varies from 0.14 mg CH_4 m^{-2} d^{-1} to 0.43 mg CH_4 m^{-2} d^{-1}, and maximum fluxes up to 1.52 mg CH_4 m^{-2} d^{-1}. These estimates are lower than ours, but higher than results by Myhre et al. (2016), also obtained in summer months.

Thornton et al. (2020) measured CH_4 flux in ESAS in July–August 2014 and obtained the range of 4.58, 1.74, and 0.14 mg CH_4 m^{-2} d^{-1} in the Laptev, West Siberian and Chukchi seas, respectively. Annual fluxes estimated from 3 satellite data sets for entire ESAS are in the range 2.8 – 6.7 mg CH_4 m^{-2} d^{-1} (Table 2).

4.2 The wintertime CH_4 anomalies over Arctic seas, their explanation, and alternative hypotheses.

A significant emission of methane from the Arctic seas in winter was speculated by Gentz et al. (2014), Myhre et al. (2016), and others. Yurganov (2020) found excess AIRS v6 and IASI CH_4 for an area south-west of Svalbard compared to North Atlantic up to 30 ppb in autumn–winter. They show that this anomaly is consistent with a fall/winter pycnocline breakdown and enhanced winter mixing. Here we present additional evidences of this effect based on improved AIRS Version 7 data, and the data of the third sounder, CrIS, retrieved using a new CLIMCAPS algorithm (Smith and Barnet, 2019, 2020). One may doubt that this extra CH_4 really emitted from the sea surface. An alternative explanation is an atmospheric advection from areas beyond the Arctic seas with higher CH_4 concentrations in winter. Tropical and sub-tropical areas are too far away, but transport of CH_4 emitted from sub-surface

layers of permafrost in cold season (Zona et al., 2016) or from leaking pipelines (IEA, 2021) cannot be ruled out. Unfortunately, TIR spectrometers are completely insensitive to lower atmospheric layers over frozen surfaces and high CH_4 concentrations in terrestrial Arctic can not be confirmed.

Our choice of data for 0–4 km of altitude was motivated by much less intensity of advection in this layer. Another argument in favor of local origin of this extra CH_4 is a natural bias of the satellite measurements: most of data are presented for clear sky or broken clouds, measurements in overcast conditions are impossible. Clear sky prevails during anticyclonic conditions with low wind speed. Also, it is known that pollutants are transported on long distances in LT mostly by cyclones (Jaffe et al., 1998). A significant duration of averaging periods (up to a few years) is another argument in favor local origin of CH_4: days with different trajectories of polluted air are mixed together. Nevertheless, this point is important and deserves a further investigation.

4.3 Winter CH_4 trends in view of the seawater mixing and ice cover.

Another point of interest is what happens with CH_4 emissions during last 20 years. As Smith and Barnet (2019, 2020) noted, analysis of satellite data, especially trends, may be ambiguous. Therefore, the data sets analyzed here (Figure 4) should be considerate with some caution. Nevertheless, comparison of two instruments with a 3-fold different spectral resolution (1.5 cm^{-1} for AIRS and 0.5 cm^{-1} for IASI) may be helpful. Note that both AIRS and IASI demonstrate similar patterns while comparing three oceanic domains (left to right in Figure 4). The difference between summer and winter (i.e., the seasonal cycle amplitude) increases from the Norwegian Sea to the western Barents Sea and then to the northern Kara Sea. The maximal statistically significant difference is observed for the IASI Kara data: the amplitude of the seasonal cycle doubled just in ten years. A high spectral resolution of IASI ensures higher sensitivity to retrieved LT concentrations (cf., Rogers, 2000). A negative trend in ice concentration (Figure 9) gives us a clue to explain this increase. The northern BKS in early winter experiences maximal decline of the ice cover from the beginning of this century. Petoukhov and Semenov (2010), Zhang et al. (2018b) found that this phenomenon significantly disturbs the air circulation in Northern mid and high latitudes. This effect could enhance transport of CH_4 through the sea/air boundary. Yurganov (2020) investigated this relationship in more detail. A positive feed-back loop between ice and methane is also possible.

Auxiliary oceanographic data may shed light on the reasons for CH_4 trends in BKS. Figure 7a clearly demonstrates variability of MLD during last 18 years and a negative trend in early winter MLD (red points). The winter/spring MLD just moderately diminished (green points). Seasonal cycles of MLD averaged over 4 years at

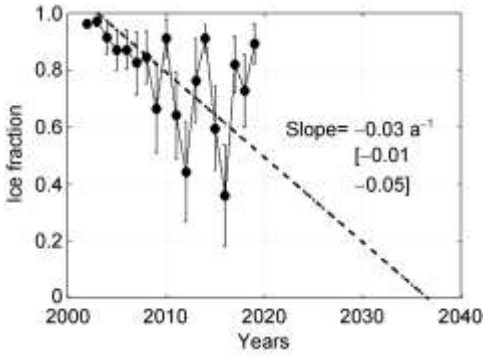

Figure 9 Ice concentration (mean fraction of area that is covered by ice) for the domain #2 (N. Kara Sea) for the November–December–January season.

the beginning and at the end of our time span (Figure 7b) may be interpreted as evolution in pycnocline breakdown date, namely, a 5-weeks shift to later time. This shift lengthens a seawater stability period allowing proliferation of methanotroph bacteria that secure oxidation of CH_4 seeped at the sea floor. This lengthening also may damp the CH_4 flux through the sea/air boundary in early winter. Freshening of the surface layer in summer (Heine et al., 2015; Yamaguchi and Suga, 2019; Li et al., 2020) may explain this effect. The steepest decline of MLD (-10 m a^{-1}) is observed in November in the Barents Sea, while the Norwegian and Kara seas do not show any significant MLD trends at all (Supplementary Figure S10).

Another important constrain is the temperature stability/instability. Dissociation rate of methane hydrates depends on the near-bottom seawater temperature. Two valuable data sets for this parameter are available now (Figure 8). Both demonstrate growing near-bottom Barents potential temperature with a rate of 0.05–0.06 ℃ a^{-1} that means ~1 ℃ warming since the beginning of this century. Methane hydrates may be impacted by this warming (Rappel and Kessler, 2016). Increased emission of gaseous CH_4 may influence the Arctic warming, providing the transport of the dissolved methane would be sufficient.

Summing up, the steepest temperature increase is observed in the Barents Sea but no or negligible increase in CH_4 amplitude is observed there. The fastest growth of the CH_4 amplitude occurs in the Kara Sea with low and constant seawater temperature. The latter may be explained by a decisive role of ice decline in the Kara Sea. In contrast to the Kara Sea, two important factors compensate one another in the Barents Sea: a positive temperature trend stimulates emission, but the freshening of the mixed layer lengthens the stratification period and hampers the CH_4 flux to the atmosphere.

According to our analysis, BKS dominates as a regional source of atmospheric CH_4 for the Arctic Ocean (Figure 6 and Table 1). This is reasonable if one takes in view abundant sea floor CH_4 sources (James at al., 2016) and influx of heat through the North–Atlantic Current

(NAC) through the Barents Sea gateway (Leifer et al. 2018). CH_4 seeps from faults, earthquakes, oil and gas deposits, high concentrations of dissolved CH_4 are observed in deep layers (Supplementary Figure S1). This CH_4 is partly converted to gas hydrate at temperatures lower than ~ 2 °C and depths below ~ 250 m (James at al., 2016; Ruppel and Kessler, 2017). Methane hydrate dissociates under the influence of AW flow (Leifer et al., 2018).

5 Conclusions

Following our analysis on the sea-air methane flux and possible modulating factors in Barrents and Kara seas based on satellite data, we could make these conclusions:

(1) Most of methane emission from BKS occurs in winter, when the whole seawater column is mixed.

(2) The amplitude of CH_4 seasonal cycle at the northern edge of BKS grows with years. A decline of sea ice that facilitates CH_4 flux to air in winter is the most likely explanation of that. Conversely, the ice-free western Barents Sea does not show any clear evidence of growing emission.

(3) CH_4 emission from the Arctic Ocean as a whole is estimated as ~2/3 of the land emission. The contribution of BKS to marine emission is between 40% and 50%.

Acknowledgments We express our gratitude to personnel of NASA and NOAA that make publicly available satellite data on methane and sea ice concentration. Colm Sweeney (NOAA/GMD, Boulder, CO) kindly supplied data of aircraft sampling over the Trinidad Head, California. We appreciate discussing some issues of our study with Nadia Smith (Science and Technology Corporation, Columbia, MD), Shamil Maksyutov (National Institute for Environmental Studies, Tsukuba, Japan), and Jean-Daniel Paris (Laboratoire des Sciences du Climat et de l'Environnement, Gif sur Yvette Cedex, France). We would like to thank the two anonymous reviewers and Associate Editor, Prof. Zhouqing Xie for their valuable suggestions and comments regarding further improvement of this article.

References

Årthun M, Eldevik T, Smedsrud L H. 2019. The role of Atlantic heat transport in future Arctic winter sea ice loss. J Clim, 32(11): 3327-3341, doi:10.1175/jcli-d-18-0750.1.

Berchet A, Pison I, Chevallier F, et al. 2015. Natural and anthropogenic methane fluxes in Eurasia: a mesoscale quantification by generalized atmospheric inversion. Biogeosciences, 12(18): 5393-5414, doi:10.5194/bg-12-5393-2015.

Berchet A, Bousquet P, Pison I, et al. 2016. Atmospheric constraints on the methane emissions from the East Siberian Shelf. Atmos Chem Phys, 16(6): 4147-4157, doi:10.5194/acp-16-4147-2016.

Bloom H J. 2001. The cross-track infrared sounder (CrIS): a sensor for operational meteorological remote sensing, in Fourier Transform Spectroscopy. OSA Trends in Optics and Photonics, 3: 1341-1343, Optical Society of America, doi: 10.1109/IGARSS.2001.976838.

Cavalieri D J, Parkinson C L, Gloersen P, Zwally H J. 1996. Sea ice concentrations from Nimbus-7 SMMR and DMSP SSM/I-SSMIS passive microwave data, Version 1. Boulder, Colorado USA. NASA National Snow and Ice Data Center Distributed Active Archive Center, doi: 10.5067/8GQ8LZQVL0VL.

Comiso J C, Parkinson C L, Gersten R, et al. 2008. Accelerated decline in the Arctic sea ice cover. Geophys Res Lett, 35(1): L01703, doi:10.1029/2007GL031972.

de Boyer Montégut C, Madec G, Fischer A S, et al. 2004. Mixed layer depth over the global ocean: an examination of profile data and a profile-based climatology. J Geophys Res: Ocean, 109(C12): C12003, doi:10.1029/2004JC002378.

Fekete B M, Vörösmarty C J, Grabs W. 2002. High-resolution fields of global runoff combining observed river discharge and simulated water balances. Glob Biogeochem Cycles, 16(3): 15-1-15-10, doi:10.1029/1999GB001254.

Fenty I, Menemenlis D, Zhang H. 2017. Global coupled sea ice-ocean state estimation. Clim Dyn, 49(3): 931-956, doi:10.1007/s00382-015-2796-6.

Ferré B, Jansson P G, Moser M, et al. 2020. Reduced methane seepage from Arctic sediments during cold bottom-water conditions. Nat Geosci, 13(2): 144-148, doi:10.1038/s41561-019-0515-3.

Forget G, Campin J M, Heimbach P, et al. 2015. ECCO version 4: an integrated framework for non-linear inverse modeling and global ocean state estimation. Geosci Model Dev, 8(10): 3071-3104, doi:10.5194/gmd-8-3071-2015.

Fung I, John J, Lerner J, et al. 1991. Three-dimensional model synthesis of the global methane cycle. J Geophys Res: Atmos, 96(D7): 13033-13065, doi:10.1029/91JD01247.

Gambacorta A. 2013. The NOAA unique CrIS/ATMS processing system (NUCAPS): algorithm theoretical basis documentation. hhttp://www.ospo.noaa.gov/Products/atmosphere/soundings/nucaps/docs/NUCAPS_ATBD_20130821.pdf

Gent P R, McWilliams J C. 1990. Isopycnal mixing in ocean circulation models. J Phys Oceanogr, 20(1): 150-155, doi:10.1175/1520-0485(1990)020<0150: imiocm>2.0.co;2.

Gentz T, Damm E, Schneider von Deimling J, et al. 2014. A water column study of methane around gas flares located at the West Spitsbergen continental margin. Cont Shelf Res, 72: 107-118, doi:10.1016/j.csr.2013.07.013.

Glagolev M, Kleptsova I, Filippov I, et al. 2011. Regional methane emission from West Siberia mire landscapes. Environ Res Lett, 6(4): 045214, doi:10.1088/1748-9326/6/4/045214.

Haine T W N, Curry B, Gerdes R, et al. 2015. Arctic freshwater export: status, mechanisms, and prospects. Glob Planet Chang, 125: 13-35, doi:10.1016/j.gloplacha.2014.11.013.

Hoegh-Guldberg O, Bruno J F. 2010. The impact of climate change on the world's marine ecosystems. Science, 328(5985): 1523-1528, doi:10.1126/science.1189930.

Höglund-Isaksson L. 2012. Global anthropogenic methane emissions 2005–2030: technical mitigation potentials and costs. Atmos Chem Phys, 12(19): 9079-9096, doi:10.5194/acp-12-9079-2012.

International Energy Agency (IEA). 2021. Methane Tracker Database, IEA, Paris. https://www.iea.org/articles/methane-tracker-database.

Jaffe D, Yurganov L, Pullman E, et al. 1998. Measurements of CO and O3 at shemya, Alaska. J Geophys Res, 103(D1): 1493-1502, doi:10.1029/

97jd02076.

James R H, Bousquet P, Bussmann I, et al. 2016. Effects of climate change on methane emissions from seafloor sediments in the Arctic Ocean: a review. Limnol Oceanogr, 61(S1): S283-S299, doi:10.1002/lno.10307.

Kara A B, Rochford P A, Hurlburt H E. 2000. An optimal definition for ocean mixed layer depth. J Geophys Res: Ocean, 105(C7): 16803-16821, doi:10.1029/2000JC900072.

Kara A B, Rochford P A, Hurlburt H E. 2002. Mixed layer depth variability over the global ocean. J Geophys Res: Ocean, 108(C3): 3079, doi:10.1029/2000JC000736.

Kort E A, Wofsy S C, Daube B C, et al. 2012. Atmospheric observations of Arctic Ocean methane emissions up to 82 °north. Nat Geosci, 5(5): 318-321, doi:10.1038/ngeo1452.

Leifer I, Chen F R, McClimans T, et al. 2018. Satellite ice extent, sea surface temperature, and atmospheric methane trends in the Barents and Kara seas. The Cryosphere Discuss, Response to Dr. Antonia Gambacorta. https://www.the-cryosphere-discuss.net/tc-2018-237/tc-2018-237-AC3-Supplementary.pdf.

Li G C, Cheng L J, Zhu J, et al. 2020. Increasing ocean stratification over the past half-century. Nat Clim Chang, 10(12): 1116-1123, doi:10.1038/s41558-020-00918-2.

Lorenson T D, Greinert J, Coffin R B. 2016. Dissolved methane in the Beaufort Sea and the Arctic Ocean, 1992–2009; sources and atmospheric flux. Limnol Oceanogr, 61(S1): S300-S323, doi:10.1002/lno.10457.

Maddy E S, Barnet C D, Gambacorta A. 2009. A computationally efficient retrieval algorithm for hyperspectral sounders incorporating A priori information. IEEE Geosci Remote Sens Lett, 6(4): 802-806, doi:10.1109/LGRS.2009.2025780.

Mau S, Römer M, Torres M E, et al. 2017. Widespread methane seepage along the continental margin off Svalbard–from Bjørnøya to Kongsfjorden. Sci Rep, 7: 42997, doi:10.1038/srep42997.

Menemenlis D, Campin J, Heimbach P, et al. 2008. ECCO2: high resolution global ocean and sea ice data synthesis. Mercator Ocean Quarterly Newsletter, 31: 13-21.

Menemenlis D, Fukumori I, Lee T. 2005a. Using Green's functions to calibrate an ocean general circulation model. Mon Weather Rev, 133(5): 1224-1240, doi:10.1175/mwr2912.1.

Menemenlis D, Hill C, Adcrocft A, et al. 2005b. NASA supercomputer improves prospects for ocean climate research. Eos Trans Am Geophys Union, 86(9): 89-96, doi:10.1029/2005EO090002.

Myhre C L, Ferré B, Platt S M, et al. 2016. Extensive release of methane from Arctic seabed west of Svalbard during summer 2014 does not influence the atmosphere. Geophys Res Lett, 43(9): 4624-4631, doi:10.1002/2016GL068999.

Nisbet E G, Manning M R, Dlugokencky E J, et al. 2019. Very strong atmospheric methane growth in the four years 2014-2017: implications for the Paris Agreement. Glob Biogeochem Cycles, 33(3): 318-342, doi:10.1029/2018GB006009.

Olivier J G J, van Aardenne J A, Dentener F J, et al. 2005. Recent trends in global greenhouse gas emissions: regional trends 1970-2000 and spatial distributionof key sources in 2000. Environ Sci, 2(2-3): 81-99, doi:10.1080/15693430500400345.

Petoukhov V, Semenov V A. 2010. A link between reduced Barents-Kara sea ice and cold winter extremes over northern continents. J Geophys Res: Atmos, 115(D21): D21111, doi:10.1029/2009JD013568.

Portnov A, Mienert J, Serov P. 2014. Modeling the evolution of climate-sensitive Arctic subsea permafrost in regions of extensive gas expulsion at the West Yamal shelf. J Geophys Res: Biogeosciences, 119(11): 2082-2094, doi:10.1002/2014JG002685.

Razavi A, Clerbaux C, Wespes C, et al. 2009. Characterization of methane retrievals from the IASI space-borne sounder. Atmos Chem Phys, 9(20): 7889-7899, doi:10.5194/acp-9-7889-2009.

Redi M H. 1982. Oceanic isopycnal mixing by coordinate rotation. J Phys Oceanogr, 12(10): 1154-1158, doi:10.1175/1520-0485(1982)012<1154: oimbcr>2.0.co;2.

Rodgers C D. 2000. Inverse methods for atmospheric sounding: theory and practice. Singapore: World Scientific, doi:10.1142/3171.

Rudels B. 1993. High latitude ocean convection//Stone D B, Runcorn S K. Flow and creep in the Solar System: observations, modeling and theory. Dordrecht: Springer Netherlands, 323-356, doi:10.1007/978-94-015-8206-3_20.

Ruppel C D, Kessler J D. 2017. The interaction of climate change and methane hydrates. Rev Geophys, 55(1): 126-168, doi:10.1002/2016rg000534.

Saunois M, Stavert A R, Poulter B, et al. 2020. The global methane budget 2000–2020. Earth Syst Sci Data, 12: 1561-1623, doi:10.5194/essd-12-1561-2020.

Serov P, Vadakkepuliyambatta S, Mienert J, et al. 2017. Postglacial response of Arctic Ocean gas hydrates to climatic amelioration. PNAS, 114(24): 6215-6220, doi:10.1073/pnas.1619288114.

Shakhova N, Semiletov I, Salyuk A, et al. 2010. Extensive methane venting to the atmosphere from sediments of the East Siberian Arctic Shelf. Science, 327(5970): 1246-1250, doi:10.1126/science.1182221.

Shipilov, E V, Murzin R R. 2002. Hydrocarbon deposits of western part of Russian shelf of Arctic – Geology and systematic variations. Petrol Geol, 36(4): 325-347 [Translated from Geologiya Nefti i Gaza, 2001, no. 4, p. 6-19].

Skagseth Ø, Eldevik T, Årthun M, et al. 2020. Reduced efficiency of the Barents Sea cooling machine. Nat Clim Chang, 10(7): 661-666, doi:10.1038/s41558-020-0772-6.

Smith N, Barnet C D. 2019. Uncertainty characterization and propagation in the Community Long-term Infrared Microwave Combined Atmospheric Product System (CLIMCAPS). Remote Sens, 11(10): 1227, doi:10.3390/rs11101227.

Smith N, Barnet C D. 2020. CLIMCAPS observing capability for temperature, moisture, and trace gases from AIRS/AMSU and CrIS/ATMS. Atmos Meas Tech, 13: 4437-4459, doi:10.5194/amt-13-4437-2020.

Susskind J, Barnet C D, Blaisdell J M. 2003. Retrieval of atmospheric and surface parameters from AIRS/AMSU/HSB data in the presence of clouds. IEEE Trans Geosci Remote Sens, 41(2): 390-409, doi:10.1109/TGRS.2002.808236.

Susskind J, Blaisdell J, Iredell L. 2012. Significant advances in the AIRS Science Team Version-6 retrieval algorithm. SPIE Optical Engineering + Applications. Proc SPIE 8510, Earth Observing Systems XVII, 85100U. San Diego, California, USA. doi:10.1117/12.929953.

Susskind J, Blaisdell J M, Iredell L. 2014. Improved methodology for surface and atmospheric soundings, error estimates, and quality control procedures: The Atmospheric Infrared Sounder science team version-6 retrieval algorithm. J Appl Rem Sens, 8(1): 084994, doi:

10.1117/1.JRS.8.084994.

Sweeney C, Dlugokencky E, Miller C E, et al. 2016. No significant increase in long-term CH_4 emissions on North Slope of Alaska despite significant increase in air temperature. Geophys Res Lett, 43(12): 6604-6611, doi:10.1002/2016GL069292.

Thornton B F, Prytherch J, Andersson K, et al. 2020. Shipborne eddy covariance observations of methane fluxes constrain Arctic sea emissions. Sci Adv, 6(5): eaay7934, doi:10.1126/sciadv.aay7934.

Tian B, Manning R J, Thrastarson H, et al. 2020. AIRS Version 7 Level 3 product user guide. https:// docserver.gesdisc.eosdis.nasa.gov/public/project/AIRS/V7_L3_User_Guide.pdf.

Watelet S, Skagseth Ø, Lien V S, et al. 2020. A volumetric census of the Barents Sea in a changing climate. Earth Syst Sci Data, 12(4): 2447-2457, doi:10.5194/essd-12-2447-2020.

Wunsch C, Heimbach P, Ponte R, et al. 2009. The global general circulation of the ocean estimated by the ECCO-consortium. Oceanography, 22(2): 88-103, doi:10.5670/oceanog.2009.41.

Xiong X, Barnet C, Maddy E S, et al. 2013. Mid-upper tropospheric methane retrieval from IASI and its validation. Atmos Meas Tech, 6(9): 2255-2265, doi:10.5194/amt-6-2255-2013.

Xiong X Z, Barnet C, Maddy E, et al. 2008. Characterization and validation of methane products from the Atmospheric Infrared Sounder (AIRS). J Geophys Res: Biogeosciences, 113(G3): G00A01, doi:10.1029/2007JG000500.

Yamaguchi R, Suga T. 2019. Trend and variability in global upper-ocean stratification since the 1960s. J Geophys Res: Ocean, 124(12): 8933-8948, doi:10.1029/2019JC015439.

Yue Q, Lambrigtsen B. 2020. AIRS Version 7 level 2 performance test and validation report. https://docserver.gesdisc.eosdis.nasa.gov/public/project/AIRS/.

Yurganov L N. 2020. The relationship between methane transport to the atmosphere and the decay of the Kara Sea ice cover: satellite data for 2003–2019, Ice and Snow. 60(3): 423-430, doi: 10.31857/S2076673420030049.

Yurganov L N, Leifer I, Myhre L C. 2016a. Seasonal and interannual variability of atmospheric methane over Arctic Ocean from satellite data. Current Problems in Remote Sensing of Earth from Space, 13(2): 107-119, doi: 10.21046/2070-7401-2016-13-2-107-119.

Yurganov L, Leifer I. 2016b. Estimates of methane emission rates from some Arctic and sub-Arctic areas, based on orbital interferometer IASI data. Current Problems in Remote Sensing of Earth from Space. 13(3): 173-183, doi: 10.21046/2070-7401-2016-13-3-173-183.

Yurganov L, Leifer I. 2016c. Abnormal concentrations of atmospheric methane over the Sea of Okhotsk during 2015/2016 winter. Curr Probl Remote Sens Earth From Space, 13(3): 231-234, doi: 10.21046/2070-7401-2016-13-3-231-234.

Yurganov L, Leifer I, Vadakkepuliyambatta S. 2017. Evidences of accelerating the increase in the concentration of methane in the atmosphere after 2014: satellite data for the Arctic. Curr Probl Remote Sens Earth From Space, 14(5): 231-234, doi: 10.21046/2070-7401-2017-14-5-248-258.

Zhang H, Menemenlis D, Fenty I G. 2018a. ECCO LLC270 Ocean-Ice State Estimate, doi:1721.1/119821.

Zhang Q, Xiao C D, Ding M H, et al. 2018b. Reconstruction of autumn sea ice extent changes since AD1289 in the Barents-Kara Sea, Arctic. Sci China Earth Sci, 61(9): 1279-1291, doi:10.1007/s11430-017-9196-4.

Zona D, Gioli B, Commane R, et al. 2016. Cold season emissions dominate the Arctic tundra methane budget. PNAS,113(1): 40-45, doi: 10.1073/pnas.1516017113.

Supplementary Figures and Tables

Supplementary Figures and Table provide additional information on methods, validity of data, flux estimates, and MT data that can be compared with LT data in the main body of the paper.

1 Example of available direct measurements of dissolved methane concentration in August/September 2012, and in August/September 2015 (Mau et al., 2017) : https://doi.org/10.1038/srep42997

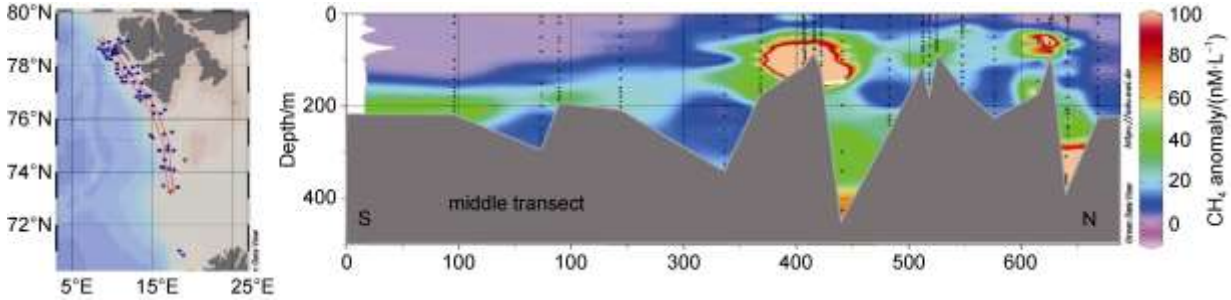

Supplementary Figure S1 South to north transect of dissolved methane concentration anomalies. Methane anomalies were derived by subtracting the atmospheric methane equilibrium concentrations from the measured methane concentrations. The left-side map indicates the transect location. May be compared with atmospheric excess CH_4 for the domain [72 °N – 74 °N, 15 °E – 30 °E] (Figure 2). Adopted from Mau et al. (2017).

2 Coverage of TIR and SWIR spectrometers: TIR IASI, LT CH_4 concentration

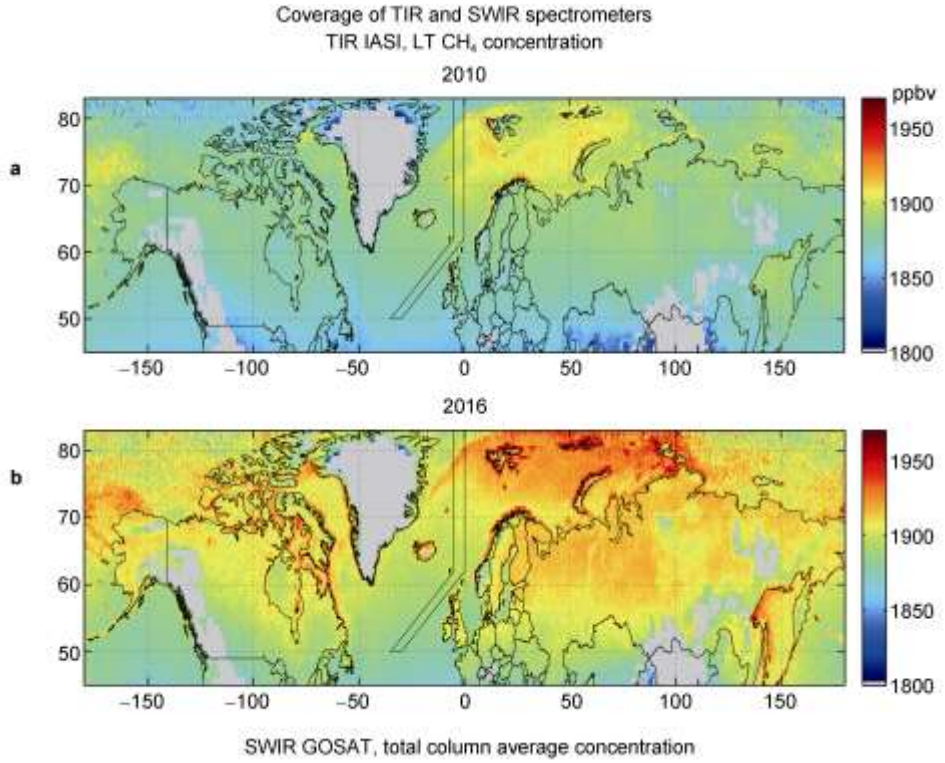

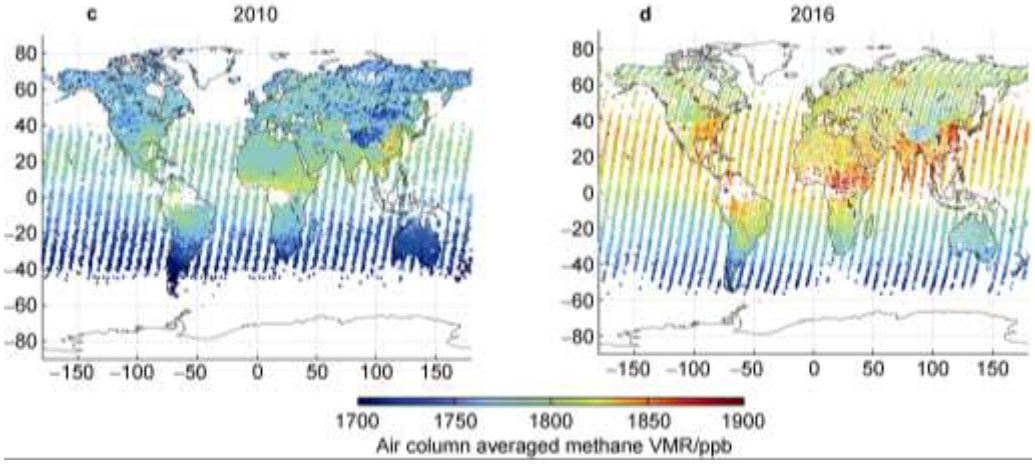

Supplementary Figure S2 Top panels. IASI annual 0–4 km average mixing ratios in 2010 (**a**) and 2016 (**b**) on the 0.5 °×0.5 ° lat./lon. grid. Maps of annual mean IASI concentration retrieved for the lower 4 km layer, data for mountains and low thermal contrast (ThC) are excluded. Note a faster growing concentration for Arctic seas compared to Northern Atlantic. Bottom panels. GOSAT Level 2 v2.72, all single retrievals for 2010 (**c**) and 2016 (**d**). The lower panels illustrate a poor coverage of GOSAT compared to IASI. Measurements over sea are available only in a glint mode and are completely missing in the Arctic due to low Sun.

3 A choice of filtering criteria to exclude data with insufficient thermal contrast (temperature difference between the surface and altitude 4 km asl) in the atmosphere

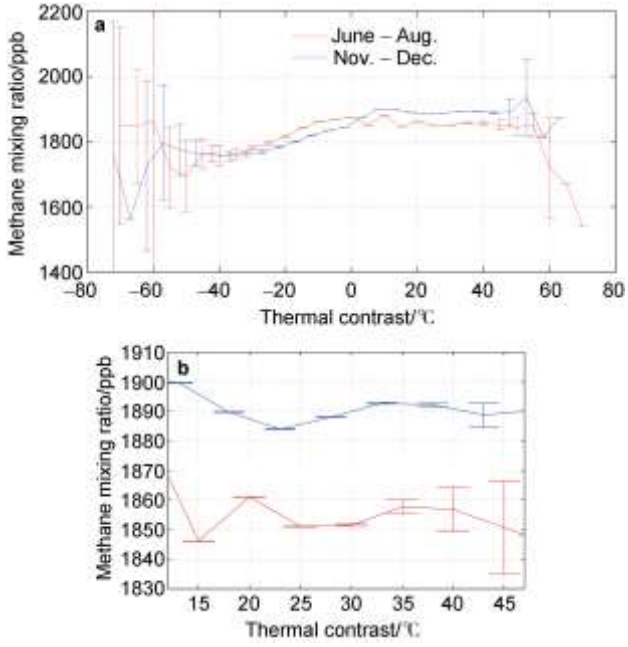

Supplementary Figure S3 A dependence of retrieved methane volume mixing ratio (VMR) on the Thermal Contrast (ThC): difference between temperatures at the surface and for air pressure 600 hPa. For ThC >10℃ this plot is flat, i.e., retrieved methane VMR does not depend on ThC. **a**, IASI lower troposphere CH_4 VMR for 2010–2016 versus ThC binned with a step 5℃. Error bars for 4*std /sqrt(N). **b**, The same, but zoomed in.

4 Two parameters characterizing sensitivity to temperature profile

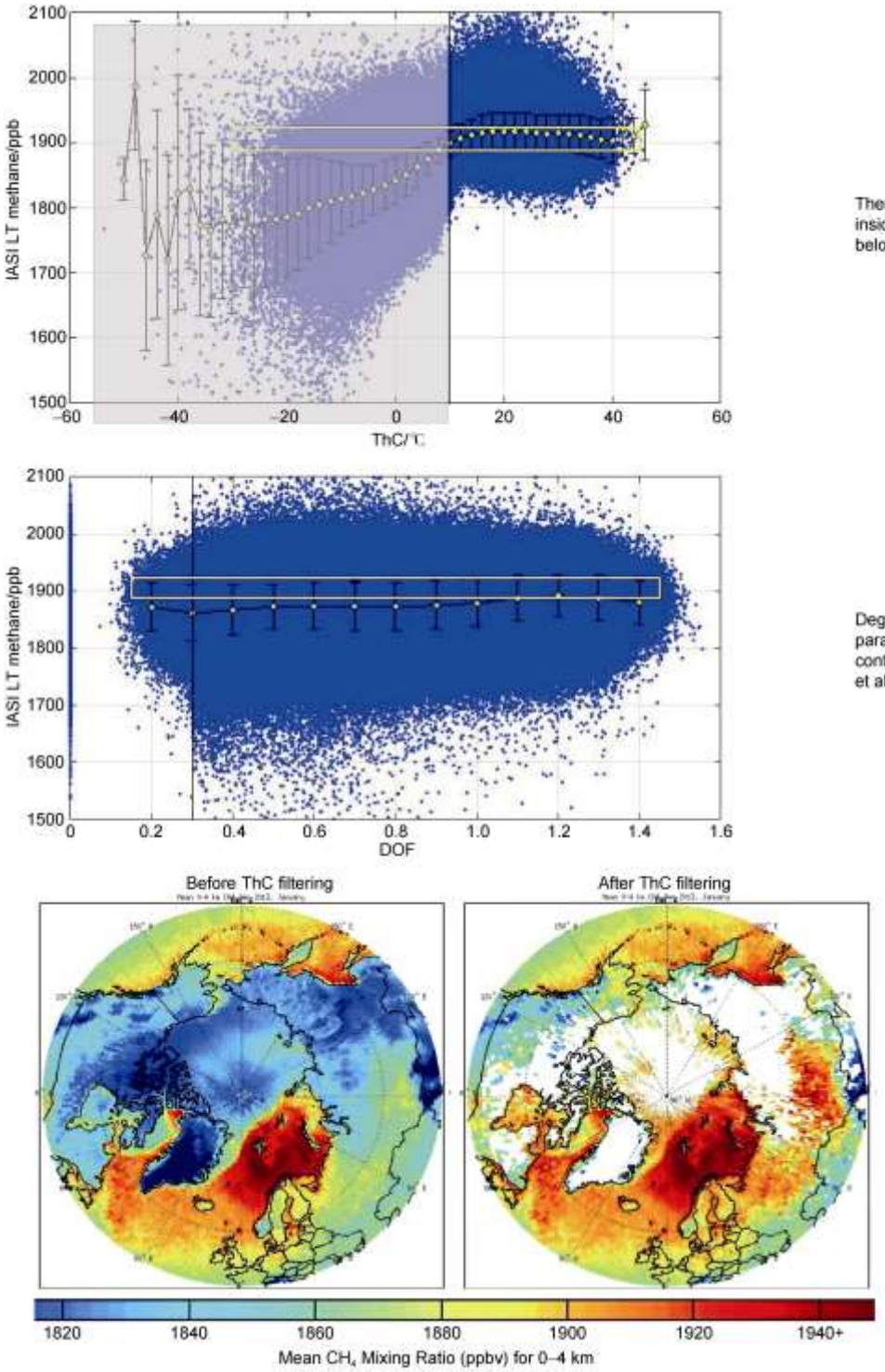

Supplementary Figure S4 Top panel. Blue points: AIRS v6 single LT retrievals in January, 2013, were plotted versus ThC and DOF. ThC=10 ℃ is a criterion for filtering. Middle panel. CH_4 is practically insensitive to DOF. Two bottom maps correspond to all points without filtering (left) and for cases ThC>10 ℃ (right). The left-side monthly mean map shows a mixture of "good" and "bad" points. Bad data are underestimated. After removal of bad data monthly means increase (South Siberia and Hudson Bay). The central and western Canadian CH_4 does not. It is because low CH_4 values there correspond to higher ThC, so the lower CH_4 in January in that area is really low, but not due to low ThC. Note that BKS data did not change: all data were good.

5 Validation of IASI and AIRS data by comparison with profiles CH_4 measured in situ from aircrafts over the NOAA site THD (Trinidad Head, California)

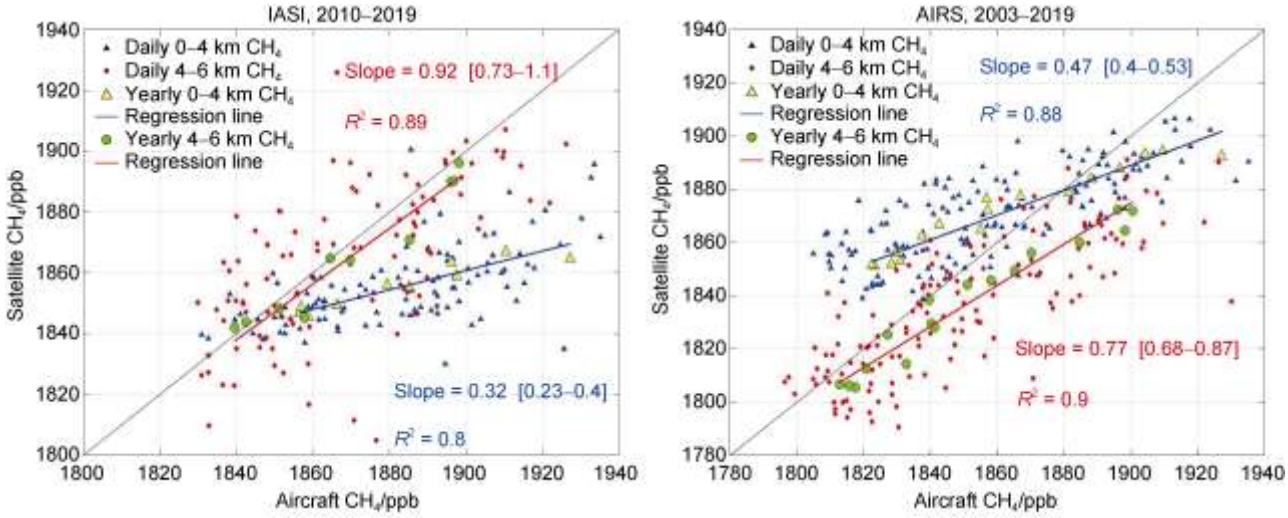

Supplementary Figure S5 CH_4 concentrations retrieved from IASI (**a**) and AIRS v6 (**b**) data on days of NOAA flights averaged in a square 150×150 km^2 centered at 41.054 ℃N, 124.151 ℃W. Triangles and circles are for annual means. Regression lines are drown through annual means. Slopes, confidence limits for reliability 95%, and regression coefficients are shown on the plots. Satellite data have a better sensitivity to mid-tropospheric CH_4 than to low tropospheric CH_4.

6 Middle tropospheric methane

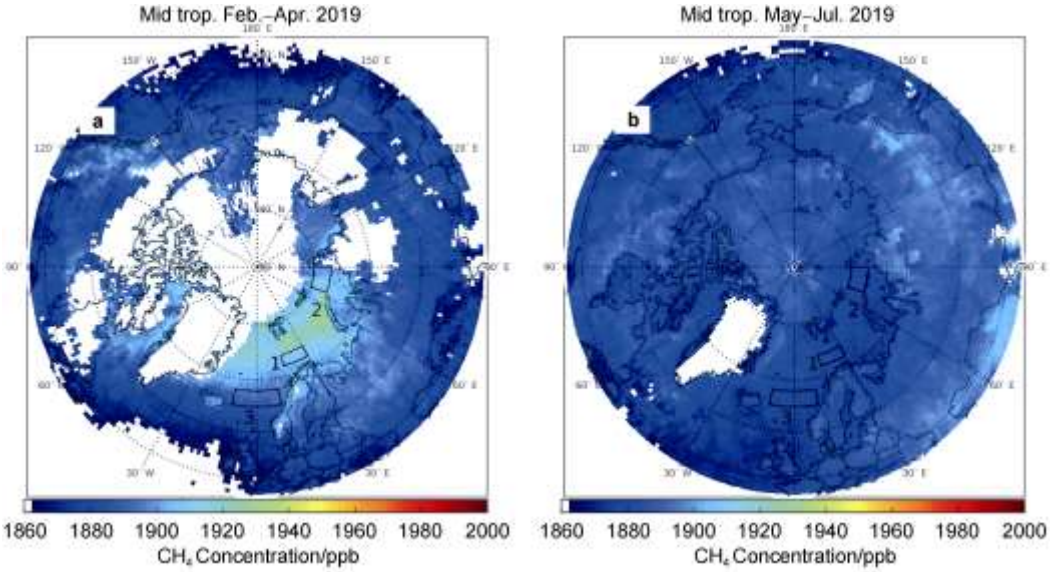

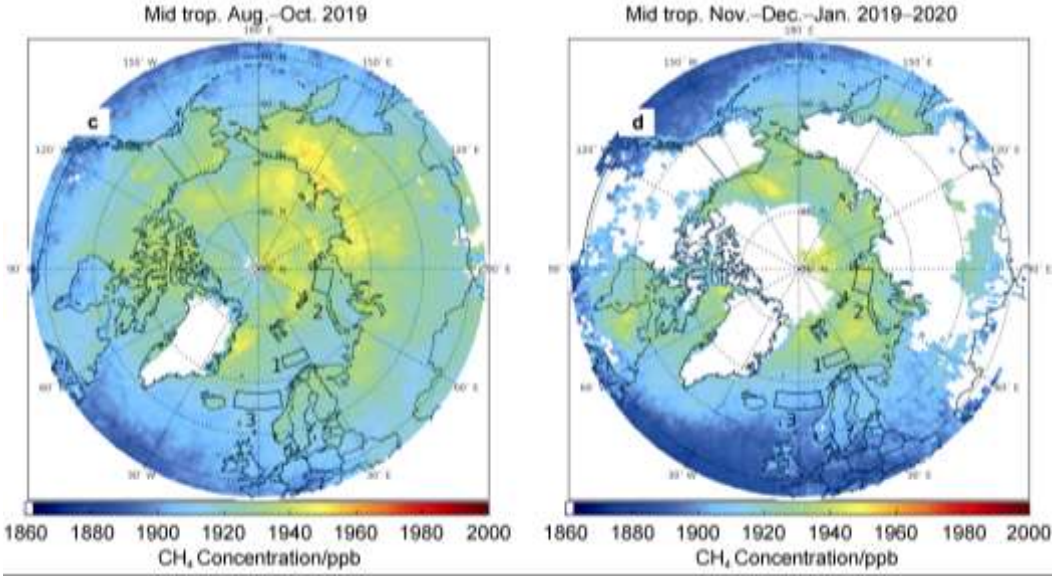

Supplementary Figure S6 Methane concentrations retrieved from data of AIRS for the mid tropospheric layer 4–6 km for 4 seasons. Blank areas correspond to insufficient vertical air temperature contrast. MT methane maps may be compared to LT (Figure 1). Note a different lower limits of the color scale for Supplementary Figure S5 and for Figure 1, upper limits are the same.

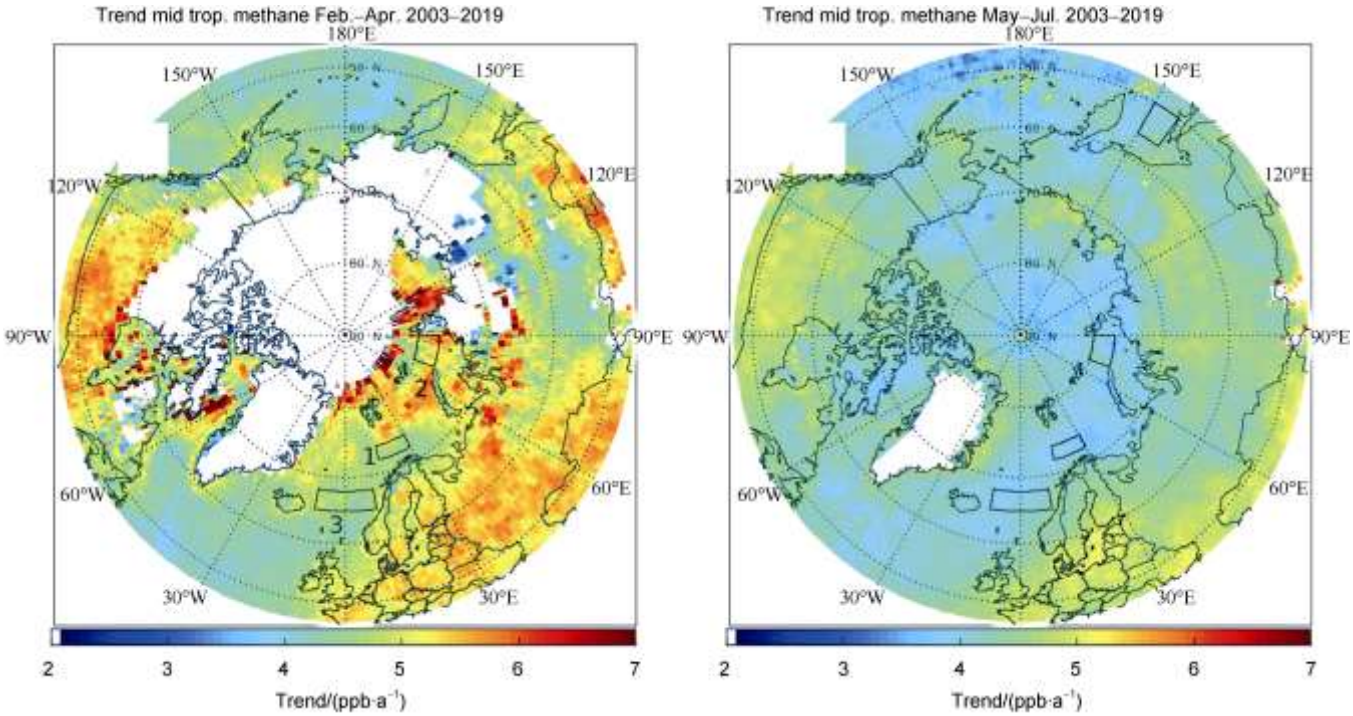

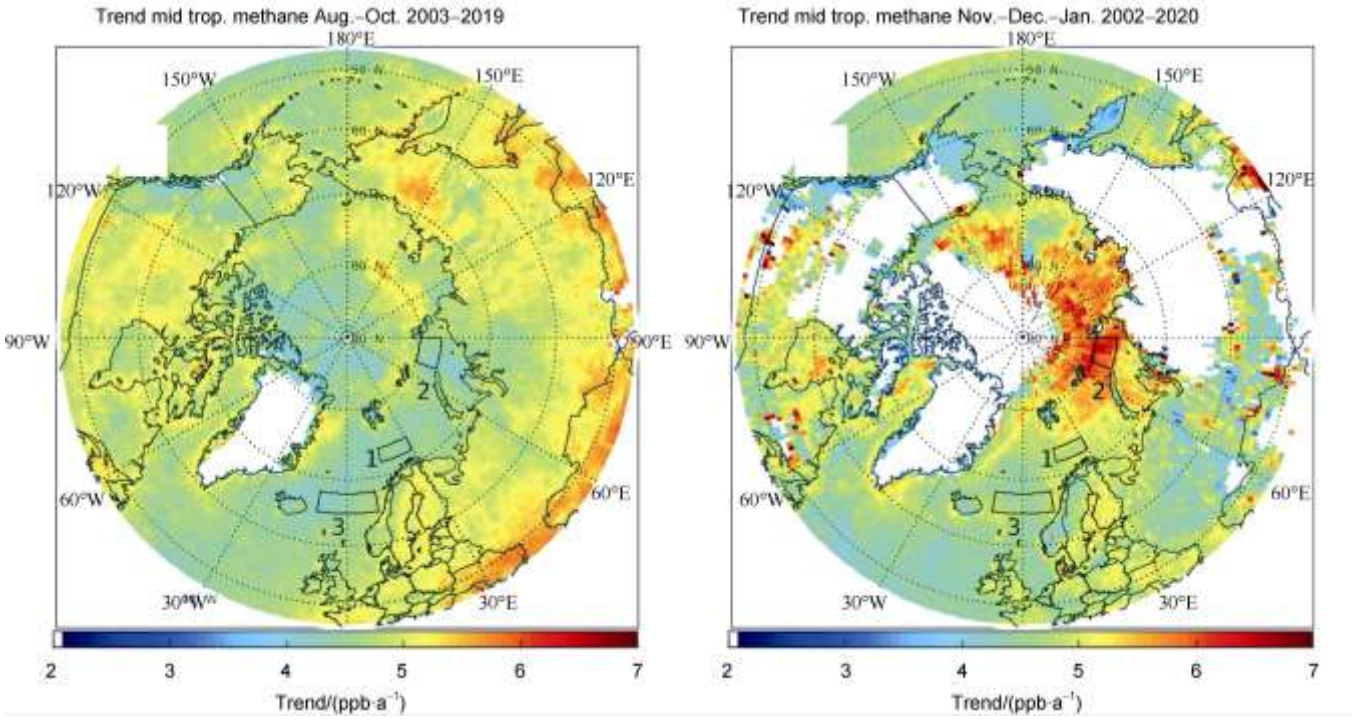

Supplementary Figure S7 Maps of mid tropospheric methane (4–6 km of altitude) trends derived from 2002–2019 data of AIRS. Slopes of standard linear regression lines for 3-month-long averaging periods (see text) were computed for methane in the layer 4–6 km and for each 1 °×1 ° lat./lon. pixel. Blank areas correspond to insufficient vertical air temperature contrast. May be compared to Figure 3 (the color scale is changed from [1:6] to [2:7] ppb a^{-1})

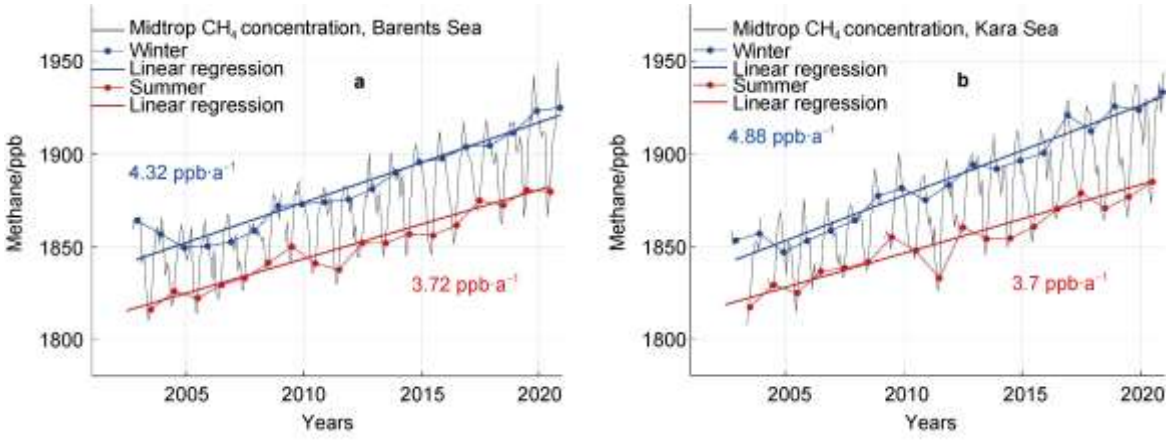

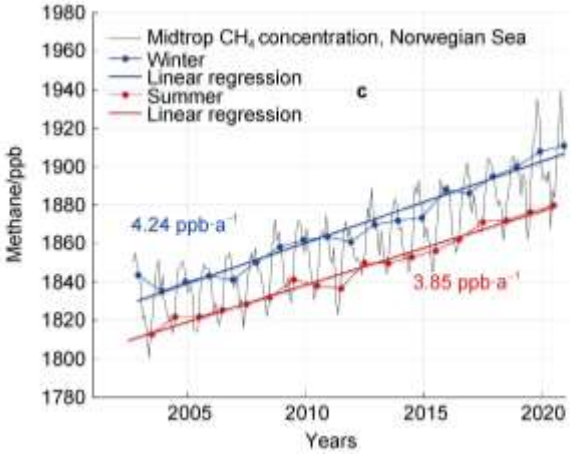

Supplementary Figure S8 Mid tropospheric methane trends according to AIRS data. Monthly mean methane concentrations for the layer 4–6 km. Domains are designated on the maps of Figure 1 and Supplementary Table S1. Regression lines are plotted for winter and summer periods, slopes are shown. May be compared to Figure 4.

7 Averaged CH_4 seasonal cycles for 3 domains

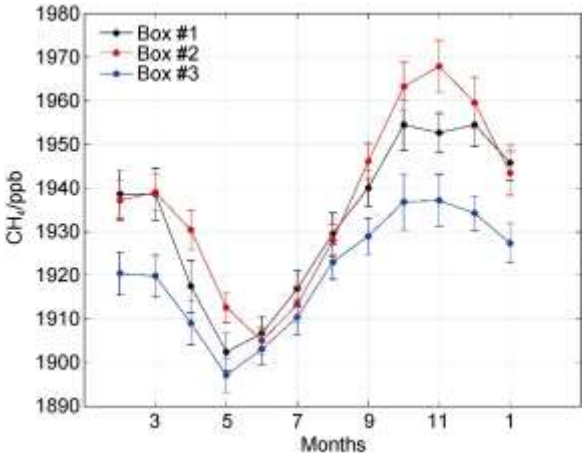

Supplementary Figure S9 Seasonal cycles of AIRS v7 LT CH_4 concentration for 3 domains, averaged over 2003–2019: Box #1 is W. Barents Sea, Box #2 is N. Kara Sea, Box #3 is Norwegian Sea. Error bars are for STD $(N\text{-}1)^{-2}$, where STD is standard deviation and *N* is number of years.

8 A choice of background concentration for calculation of CH_4 anomaly and mean annual flux density

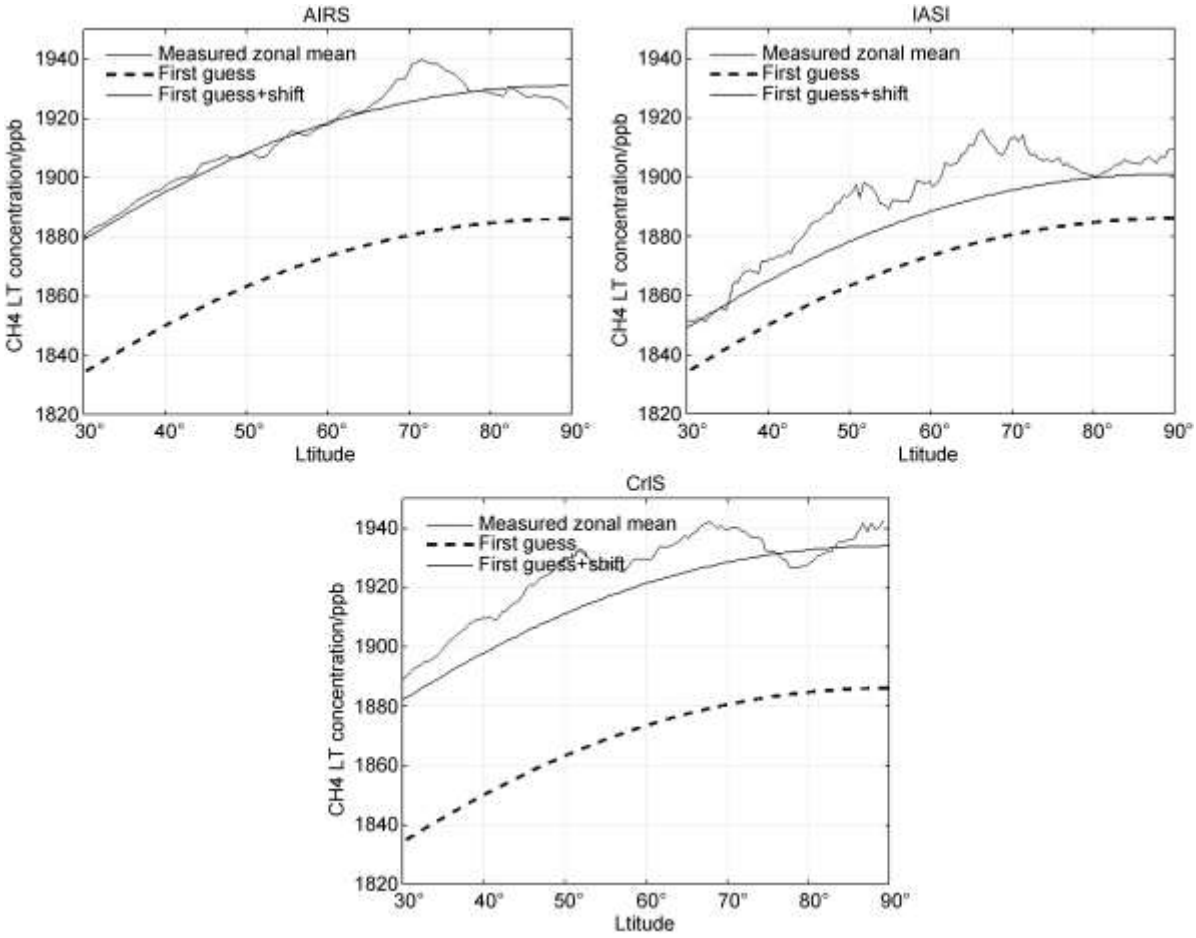

Supplementary Figure S10 Dashed line is 0–4 km mean CH_4 concentration, that is calculated from the first guess (a priori) CH_4 profiles used in retrieval algorithms for all three instruments. Blue lines are measured zonally means averaged over 2015–2020. Solid black lines are first guess adjusted for trend.

9 Negative MLD trend for the Barents Sea during late autumn – early winter and low trends for other domains

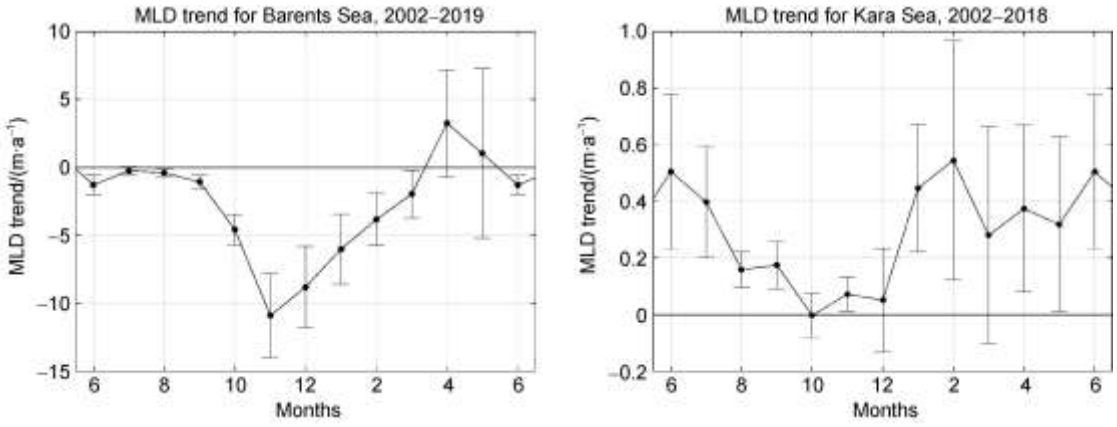

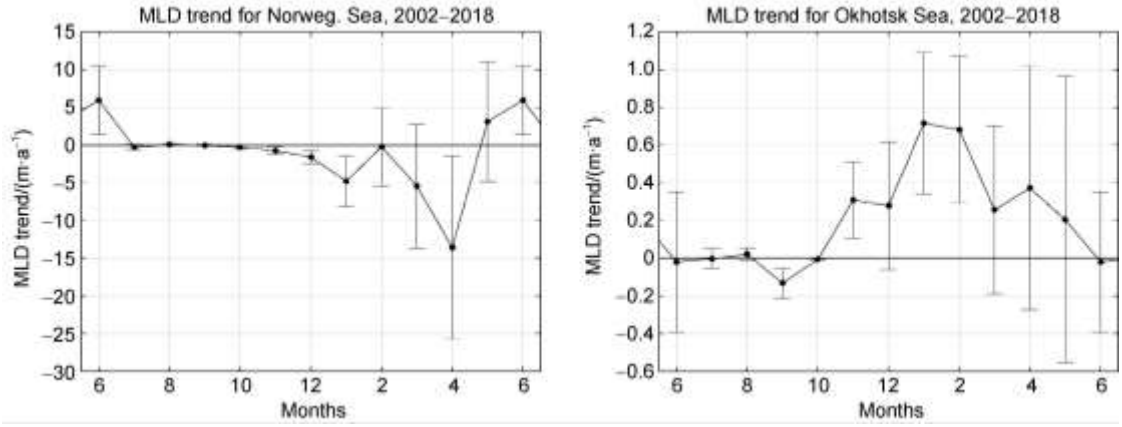

Supplementary Figure S11 Monthly ECCO MLD slopes of least square linear regression for 4 domains. Error bars are lower and upper confidence limits for reliability 95%. Note different scales.

10 Low volume of data in winter (note a log scale)

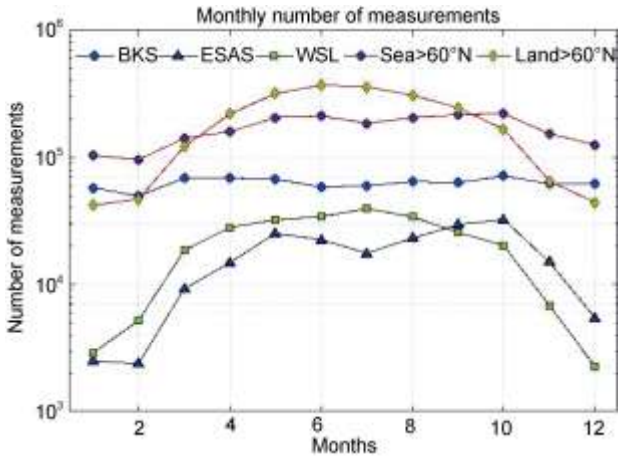

Supplementary Figure S12 Numbers of IASI measurements per month after filtering averaged for 2016–2020 in domains (see Supplementary Table S1 for boundaries).

Supplementary Table S1 Domain boundaries

	Latitude range		Longitude range	
#1 Barents Sea	72 °N	74 °N	15 °E	30 °E
#2 Kara Sea	77 °N	80 °N	70 °E	90 °E
#3 Norwegian Sea	58 °N	65 °N	10 °W	10 °E
BKS (sea only)	65 °N	82 °N	10 °W	90 °E
ESAS (seaonly)	65 °N	80 °N	120 °E	180 °E
OKH	50 °N	56 °N	144 °E	150 °E
WSL	50 °N	67 °N	60 °E	80 °E